A LINEAR MULTIPLEXED ELECTROSPRAY THIN FILM DEPOSITION SYSTEM

by

BRANDON H. LOJEWSKI
Bachelor of Science in Mechanical Engineering
University of Central Florida, 2010

A thesis submitted in partial fulfillment of the requirements
for the degree of Master of Science of Mechanical Engineering
in the Department of Mechanical and Aerospace Engineering
in the College of Engineering and Computer Science
at the University of Central Florida
Orlando, Florida

Spring Term
2013

ABSTRACT

Liquid spray is essential to industries requiring processes such as spray coating, spray drying, spray pyrolysis, or spray cooling. This thesis reports the design, fabrication, and characterization of a thin film deposition system which utilizes a linear multiplexed electrospray (LINES) atomizer. First, a thorough review of the advantages and limitations of prior multiplexed electrospray systems leads to discussion of the design rationale for this work. Next, the line of charge model was extended to prescribe the operating conditions for the experiments and to estimate the spray profile. The spray profile was then simulated using a Lagrangian model and solved using a desktop supercomputer based on Graphics Processing Units (GPUs). The simulation was extended to estimate the droplet number density flux during deposition. Pure ethanol was electrosprayed in the cone-jet mode from a 51-nozzle aluminum LINES atomizer with less than 3% relative standard deviation in the D_{10} average droplet diameter as characterized using Phase Doppler Interferometry (PDI). Finally a 25-nozzle LINES was integrated into a thin film deposition system with a heated, motion controlled stage, to deposit TiO_2 thin films onto silicon wafers from an ethanol based nanoparticle suspension. The resulting deposition pattern was analyzed using SEM, optical profilometry, and macro photography and compared with the numerical simulation results. The LINES tool developed here is a step forward to enabling the power of electrospray for industrial manufacturing applications in clean energy, health care, and electronics.

Dedicated to my best friend, Nancy Fuentes.

ACKNOWLEDGMENTS

Dr. Weiwei Deng has been an incredible advisor and influential mentor. Without his guidance and support, this work would not have been possible. I deeply appreciate your patience and diligence in guiding me towards becoming a professional researcher and engineer. I am also extraordinarily grateful for my opportunity to work with Dr. Deng shortly after he completed his seminal work on the Fundamentals and Applications of Multiplexed Electrosprays; I am standing on the shoulders of giants.

Special thanks to my first lab mate, Thomas Yang, for being my on-call physicist to answer tough questions regarding the universe, contributing to discussions about the nature of electrospray, and preparing the incredible GPU simulation work.

I must thank Dr. Cheng Li, for being my on-call materials scientist, her incredibly diligent work helped me with the deposition experiments and SEM imaging presented here.

Special thanks to Jian Liu of the UCF RISE Lab for many discussions and hours of development working beside me for the precision machining process used to fabricate the multiplexed electrospray nozzles presented in this work.

I express my deepest gratitude to my lab mates, Honxu Duan, Michael Tullbane, Johan Rodriguez, Fidelio Sime Segura, and Yan Wei. At times you all must have despised the noise pollution I created while machining components and nozzles. Although I created an environment squalid for concentrating, but you all worked countless hours though the rumbling spindle,

squealing stepper motors, and screeching metal cuts without giving me a hard time. For that you deserve huge praise.

Thank you to my family and friends for supporting me through the years during my thesis work; for always praising my ideas and listening to the grueling details. Because of you all, I have been inspired to embark on this journey and remained motivated to push through to its completion.

TABLE OF CONTENTS

LIST OF FIGURES

LIST OF TABLES

CHAPTER 1: INTRODUCTION

Liquids, solids, and gases are the three fundamental states of matter that make up everything we know. Solid matter is the state embodied by a vast majority of value added products, especially high-technology devices such as solar cells, solid state lights, and lithium-ion batteries. These solid materials are usually not found in nature and are manufactured in their functional form as 2D films, 1D fibers, or 0D particles in these devices. The field of thin film technology describes such manufacturing processes. They can be generalized as: deposition (material addition), etching (material removal), and patterning (geometric layout) (Smith 1995, Sundaram 2006).

Deposition is where the precursor elements are brought together under the right conditions to synthesize the solid material. In semiconductor manufacturing, exotic materials and nanometer tolerances are a standard practice by utilizing chemical vapor deposition (CVD) (Dobkin and Zuraw 2003) and physical vapor deposition (PVD) (Mattox 2010). In CVD, precursor vapor molecules are delivered to the substrate and chemically reacted with substrate molecules and or other vapor molecules. In PVD, solids are either thermally evaporated or physically dislodged by plasma (sputtered), to generate a flux of vapor which is brought to a surface to grow the thin film. In both PVD and CVD, the solid layers are grown from individual atoms or molecules, and in this sense, utilizing the smallest possible building block for a thin film.

Low pressure vacuum chambers are utilized in CVD and PVD processes to ensure chemical purity, film adhesion, residual stress control, submicron film thicknesses, multilayer structures, and low gas entrapment levels (Biltoft 2002). Moreover, low pressure creates a larger mean free path for vapor molecules. When the distance between the vapor source and substrate is smaller

than the mean free path, the probability of vapor molecules colliding with the substrate is maximized (Sundaram 2006). To create a vacuum environment, a well-sealed chamber must be pumped to low pressure. The pumping time and energy required to achieve and sustain low vacuum pressures contributes to at the high cost for semiconductor manufacturing, not to mention the complexities and high cost of vacuum chamber feedthrough components required for introducing vapors, motion control, heating, and other practical system design constraints.

The same CVD and PVD techniques for manufacturing microchips is also the state of the art for devices like solar cells, solid state lights, and lithium-ion batteries. However, such devices require areas that are orders of magnitude larger. The low deposition rate and high volume demand coupled with high capital equipment and operating costs have prevented scaling up production for large area thin film devices, whereas CVD and PVD are economically viable for semiconductor manufacturing because thousands of chips can be fabricated onto a single silicon wafer.

Synthesizing complex materials into films with lower amounts of energy and lower cost precursors will open up economically viable routes to manufacturing large area, thin film devices. The closer the process environment conditions are to ambient conditions, the better. The fewer steps required to refine precursors into their usable form, the better. In any case, forming a solid film will require a process where precursors are subjected to a series of temperature, pressure, and electric fields to attain the final solid product. Unlike solids however, liquids and gases are attractive precursor phases from a process standpoint since they are convenient for mixing, dispensing, spreading and are readily transported by means of pipes and tubes at atmospheric conditions. Moreover, liquids can dissolve solids, e.g. salt or sugar in water, or suspend solid

particles, e.g. sand in water. Thus, liquids can serve as a stepping stone in chemical or physical processes which link the conversion of feedstocks into value added solid products.

Spraying, in many cases, is the final step of converting a liquid to a solid, e.g. spray drying milk powder or spray painting. This work develops a new approach to liquid spraying, specifically, multiplexed electrospray (Bocanegra 2006, Deng 2009, Lojewski 2012). Electrospray is a curious spraying technique, in its ability to provide tiny, electrically charged droplets with high size uniformity at ambient conditions, in a wide size range, from 10's of nanometers to 100's of microns (Rosell-Llompart 1994, Tang 1994, Chen 1995). In certain cases, electrospray can convert liquid phase ions into gas phase ions (Fenn, et al. 1989), which might, one day, find use as the atomic building blocks for growing high quality thin films at ambient conditions (Saf, et al. 2004). In this work, a linear multiplexed electrospray system (LINES) is developed for spray coating TiO_2 nanoparticle films.

1.1 Hydrothermal Spray Synthesis

Hydrothermal synthesis broadly refers to the process of chemical reactions occurring within a solvent above room temperature. Hydrothermal synthesis is widely used to produce nanomaterials because liquid phase solution chemistry enables precise control of the reaction stoichiometry and environment conditions, i.e. concentration, temperature, pressure, electric field, etc. A temperature-pressure map for various materials synthesis techniques are shown in Figure 1,

which depicts the hydrothermal approach as requiring the lowest temperature and pressure (Byrappa and Adschiri 2007).

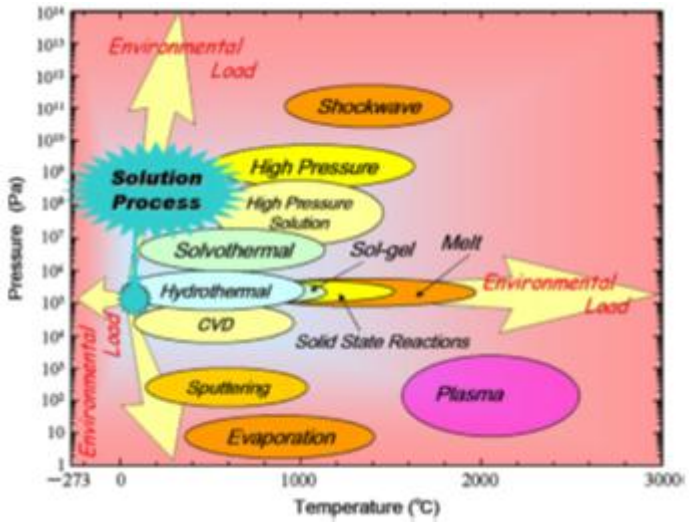

Figure 1: Pressure versus temperature map qualitatively illustrating the environmental load of numerous materials processing techniques. (Byrappa and Adschiri 2007)

Combining hydrothermal synthesis with spraying, leads to hydrothermal spray synthesis. Liquid droplets generated by spray are indispensable for accelerating hydrothermal synthesis and converting liquids into particles and films. Droplets benefit from increased surface area to volume ratios, which enable fast reaction kinetics and solvent evaporation (Som and Dash 1993). When the solvent of a solution evaporates, a discrete solid particle is formed. This technique is known as spray drying, or in the case where there is also thermal decomposition of organic molecules, spray pyrolysis. Similarly, sprayed droplets can land on a surface to grow a film. Dimensional control

over liquid droplet size is crucial to dimensional control over the solid particle or film. Droplet size can be controlled by modifying the spray nozzle operating parameters. However, as will be discussed in the next section, not all spray nozzles have the same capability. The nozzle's resulting droplet size distribution is crucial to determining the resulting product quality and manufacturing capability. This becomes especially apparent when a nanometer length scales are required.

It has been promulgated by many, and by evidence of the nano-boom in academic literature, that matter at submicron length scales leads to exciting physical and chemical phenomenon applicable to energy, medicine, and electronics (Jaworek 2008). These effects are usually due to the area to volume ratio scaling effects and the fact that the nanometer scale bridges the atomic and macro worlds. For example, in energy applications, nanotechnology lends itself to performance enhancements in solar cells, fuel cells, rechargeable batteries, supercapacitors, and hydrogen transport and storage (Serrano, Rus and Garcia-Martinez 2009). In medicine pharmaceutical nanoparticles can be tailored for enhancing the bioavailability and efficacy of drugs (Shokeen 2012). In semiconductor technology, nanowires have enabled the use of quantum bits to promise the continued improvement and miniaturization for electronics (Goodnick, et al. 2010). Although the trends in nanotechnology promise technological advancements by leaps and bounds in the fields of energy and medicine, the large scale deployment of nanotechnology has been hindered by difficulties in economically and sustainably scaling up manufacturing processes to volumes significant for industrial applications. For nanotechnology to benefit life on earth, new tools are needed which can meet the demands of manufacturing high-quality nanoparticles and thin films at large volumes and low cost.

1.2 Electrospray Advantages and Limitations

Electrohydrodynamic spray, or electrospray, is a fascinating liquid atomization method which, when operated in the cone-jet mode, naturally generates well-dispersed, non-agglomerated, liquid droplets of high size uniformity (Cloupeau and Prunet-Foch 1989). Very uniquely, the diameter of electrosprayed droplets can be controlled from nanometers to hundreds of micrometers (Tang 1994). The electrohydrodynamics (EHD) governing liquid atomization in electrospray completely differentiates it from inertia based atomization techniques such as pneumatic and ultrasonic spray. This distinction enables a new realm of size uniformity and quality control below the micron diameter bottle-neck of these traditional spray methods. Although electrospray has desirable characteristics for hydrothermal spray synthesis, the flow rate attainable for existing electrospray systems is miniscule (~1 ml/hr) (Gomez, et al. 1998) and has so far prevented the technique's deployment for industrial manufacturing.

Typically, electrospray droplets are generated by feeding a liquid connected to a high voltage power supply through a capillary column. Upon application of an electric field between the liquid and counter electrode, ions accumulate on the liquid surface at the capillary tip. When the electric field becomes intense enough, the electrostatic pressure from ion accumulation overcomes the liquid surface tension. This pulls the spherical meniscus into a cone, termed Taylor cone. A jet emanates from the cone tip and breaks up to form a cascade of electrically charged droplets. The droplets self-disperse due to Coulombic repulsion amongst each other, while also being accelerated towards the counter electrode. This results in a diverging spray profile, of either approximately parabolic or conical shape, depending upon the electrode geometry (Yang, et al.

2012). The net charge carried by droplets is transported by ions in the liquid and is equivalent to the current provided by the high voltage power supply.

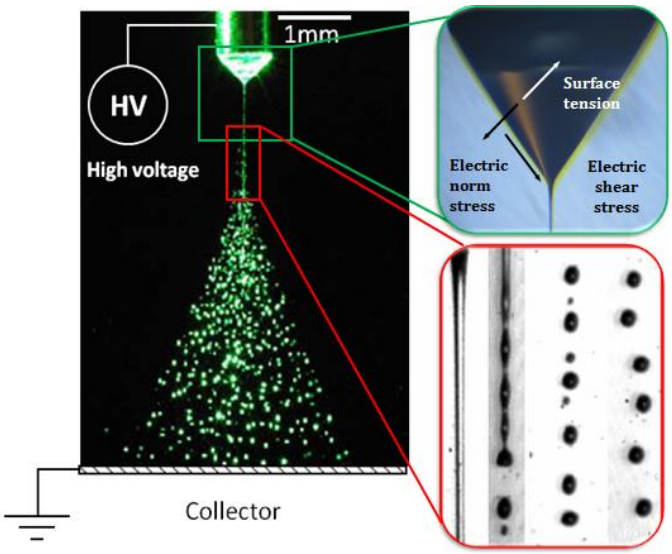

Figure 2: Overview of a single nozzle electrospray system. Zoomed in view of Taylor cone showing the vectors of surface tension, electric norm stress and shear stress (top right). Zoomed in view of jet break up (bottom right).

1.3 The Need for Multiplexed Electrospray

To preserve the advantages associated with electrospray's small and uniform droplet size yet overcome the bottleneck of low processing rate, increasing the number of spray sources, or multiplexing, becomes indispensable. Considering industrial processing rates are on the order of liters per minute, scaling up electrospray from milliliters per hour will require thousands of nozzles, depending on the liquid and application. A MES device of this order of magnitude poses

significant challenges in terms of the mechanical design, electromechanical design, fabrication, and understanding the intricacies of operating a massive amount of nozzles. A reliable MES design with a flexible and scalable fabrication process is critical.

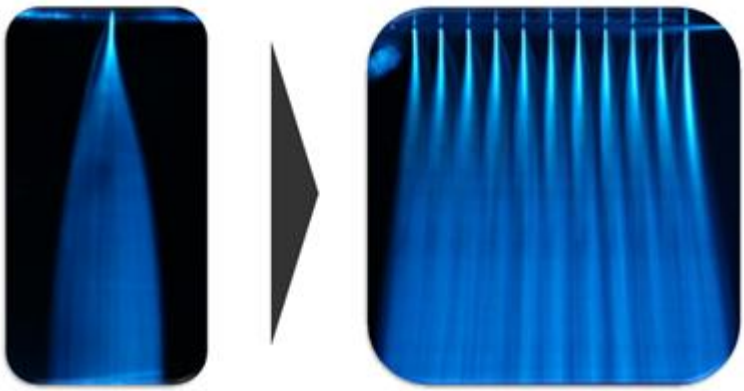

Figure 3: The need for MES. Single nozzle electrospray operating at liters per year (left). Multiplexed electrospray nozzle operating at liters per minute (right). (Deng, Klemic, et al. 2006)

1.4 Review of MES Systems

MES designs published previously show various electrode configurations and fabrication techniques, which are summarized in terms of nozzle material and the key device parameters; nozzle inner diameter (ID), channel length (L), distance between nozzles (P), and number of nozzles in the array (n). There are two main electrode configurations: two-electrode (emitter-collector) and three-electrode (distributor-extractor-collector) (Deng 2006, Bocanegra 2006). The three-electrode configuration is crucial to enabling operation of high nozzle packing densities in

the cone-jet mode since it effectively divides the device into two electric field regions to mitigate space charge issues (Deng 2007).

Device fabrication methods can be divided into 1) brute force, where multiple individual capillaries are integrated together into a single device, 2) silicon microfabrication, where devices are micromachined using photolithography for patterning with subsequent chemical etching or deposition, 3) soft lithography, where polymer devices are replicated by casting or stamping into a master mold, and 4) traditional machining, where devices are cut out using conventional drilling and milling machining techniques.

1.4.1 Brute Force

Brute force techniques assemble individual needles together on a common support. A summary of the various materials, fabrication approaches, and nozzle characteristics for the brute force techniques are provided in Table 1. Images of the brute force nozzles are also provided in Figure 4. Rulison and Flagan (1993) mounted eight stainless hypodermic needles between two aluminum angle beams with individual fluid lines connected to each nozzle. They were able to operate in the cone-jet mode using a two electrode configuration while studying the onset voltage of the array at varying capillary radius to spacing ratios. Regele et al (2002) used an array of four stainless steel hypodermic needles with 0.8mm ID arranged with a spraying needle at the center of three needles located at the vertices of an equilateral triangle. They also studied the effect of capillary spacing on the onset voltage for cone-jet mode operation of the center nozzle. Hubacz

and Marijnissen (2003) mounted four stainless steel capillaries on a Teflon plate, and showed edge effect control by adding dummy nozzles in addition to control over the spray cloud through the use of two extra electrodes. Jaworek et al (2006) mounted four stainless steel capillaries on a brass tube as a common reservoir for the nozzles, and operated with water at high flow rates (~250 ml/hr/nozzle) in the 'precession mode'. They used a three electrode configuration and studied the effect of various extractor electrode geometries. We note the largest level of multiplexing published for brute-force techniques was a modest 19 nozzles, as in Kelly et al (2008). The inherent assembly and plumbing complications with the brute force technique make scaling up to more than 100's of nozzles impractical.

Table 1: Characteristic summary for brute force MES approaches

Year	Authors	Configuration	Nozzle Material	n	P	ID	L
1991	Snarski and Dunn	Linear	Stainless Steel	2	1mm and 3mm	216µm	1.91cm
1993	Rulison and Flagan	Linear	Stainless Steel	8			
2002	Regele et al	Triangular	Stainless Steel	1	5 to 20mm	800µm	10cm
2003	Hubacz and Marijnissen	Linear	Stainless Steel	4	1cm		3.3cm
2006	Jaworek et al	Linear	Stainless Steel	4	30mm	500µm	10mm
2007	Si et al	Linear	Stainless Steel	3	1 to 20mm	500µm	
2008	Kelly et al	Linear	Fused silica	19	0.5mm and 1mm	20µm	4cm
2008	Kelly et al	Circular	Fused silica	19	500µm	20µm	30mm

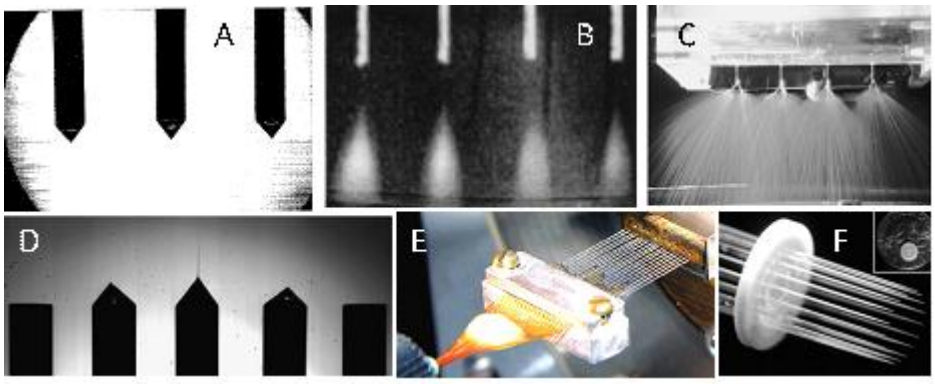

Figure 4: Images of brute force MES nozzles. A - (Rulison and Flagan 1993), B - (Hubacz and Marijnissen 2003), C - (Jaworek, Lackowski, et al. 2006), D - (Tran, Byun and Lee 2007), E - (Kelly, Page and Zhao, et al. 2008), F - (Kelly, Page and Marginean, et al. 2008)

1.4.2 Silicon Microfabrication

Silicon microfabrication uses photolithography to pattern submicron tolerances. Moreover, the parallel nature of the process makes it well suited for producing large numbers of nozzles. This led Deng et al (2009) to demonstrate 10,000 sources/cm^2, as well as an increase in throughput by two orders of magnitude while preserving the monodispersity (Deng et al, 2008). This system was successfully applied in a high power-density liquid fuel micro-combustor (Deng et al. 2007), synthesis of biodegradable PLGA micro and nano particles (Almeria et al. 2010, 2011), and an ion thruster for compact space propulsion (Lenguito et al, 2010). A summary of the various materials, fabrication approaches, and nozzle characteristics for the silicon microfabrication techniques are provided in Table 2. Images of the numerous silicon microfabricated MES nozzles are provided in Figure 5. Velásquez-García and Ibitayo (2006) also microfabricated silicon nozzles for thruster applications but instead used a linear nozzle array with a slot extractor. Disadvantages with silicon microfabrication lie in the cost and complexity of the process; each device design requires a unique set of photolithography masks for patterning, the material removal depends on the chemistry of the etching process, usually limiting device materials to silicon. Moreover, the capital equipment and overhead cost of a cleanroom microfabrication facility is limiting.

Table 2: Characteristic summary for silicon microfabrication MES approaches

Year	Authors	Configuration	Nozzle Material	n	P	ID	L
1997	Xue et al	Linear	Glass	8	6mm	60µm x 25µm	3.5-5mm
1999	Wang et al	Linear	Parylene, Photoresist, SiN	3	5cm	5µm x 10µm	2.5mm
2002	Tai et al	Linear	Parylene	3	5cm	5µm x 10µm	2.5mm
2006	Deng et al	Hexagonal planar	Silicon	91	675µm	120µm	
2006	Velásquez-García et al	Linear	Silicon	240	130µm	12µm	15mm
2007	Kim et al	Linear	Silicon	10	10µm	100µm x 8µm	~5cm
2011	Mao et al	Circular	Silicon	960	2mm	400µm x 10µm	~20mm

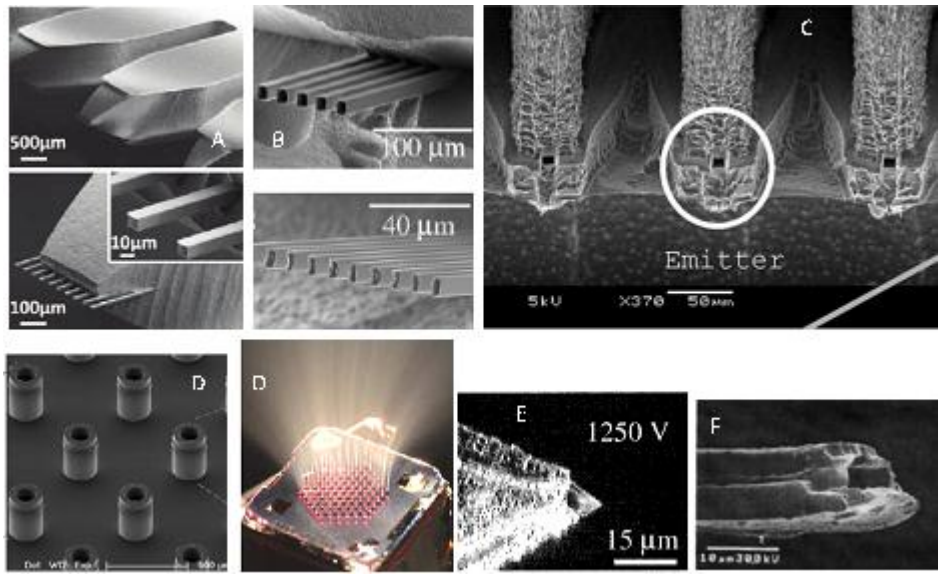

Figure 5: Images of silicon microfabrication MES nozzles. A - (Mao, et al. 2011), B - (Kim, et al. 2007), C - (Velásquez-García, Akinwande and Martínez-Sánchez 2006), D - (Deng, Klemic, et al. 2006), E - (Wang, et al. 1999), F - (Tai, et al. 2002).

1.4.3 Soft Lithography

In soft lithography a pattern can be replicated from a master mold, which must be fabricated prior to casting or stamping the device. Soft lithography lies in between silicon microfabrication and traditional machining, in the sense that first, fabrication of master mold will be performed using either silicon microfabrication or precision machining. Typically the casted component is a polymer such as poly(methyl methacrylate) (PMMA) or poly(dimethylsiloxane) (PDMS) which is cast in liquid state, molded or stamped, then hardened into a solid part. A summary of the various materials, fabrication approaches, and nozzle characteristics for the soft lithography techniques are provided in Table 3. Images of some of the soft lithography MES nozzles can be seen in Figure 6. Kim et al (2001) demonstrated a 16-channel miniaturized electrospray emitter for ESI-MS. Choi et al (2011) demonstrated a hybrid emitter with 3 nozzles using a PDMS base containing micro channels with glass capillaries inserted. The flow rate and potential of each nozzle could be addressed individually and the authors reported the cross-talk effect between nozzles at varying operating conditions.

Table 3: Characteristic summary for soft lithography MES approaches

Year	Authors	Configuration	Nozzle Material	n	P	ID	L
2001	Kim et al	Linear	PDMS	16	1.2mm	30µm	1mm
2011	Choi et al	Linear	Glass capillaries in PDMS	3	3-5mm	750µm	1-2cm

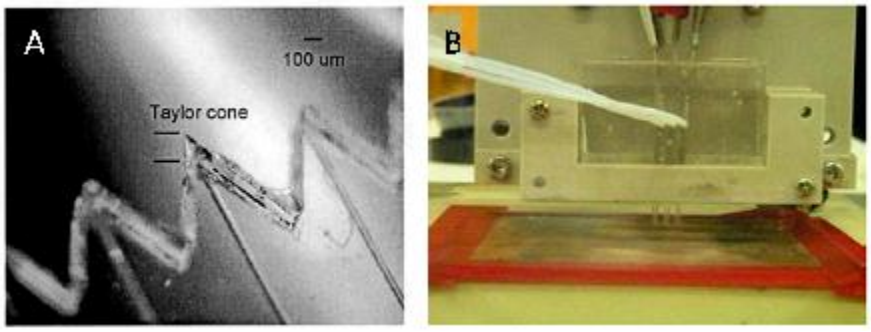

Figure 6: Images of soft lithography MES nozzles. A - (Kim and Knapp 2001), B - (Choi, et al. 2011)

1.4.4 Traditional Machining

In terms of rapid prototyping, traditional machining is the most convenient technique for implementing design changes. This is because computer drawings and machine toolpaths can be regenerated as needed and devices can be fabricated in most machinable materials with micron-level precision. The resolution depends on the accuracy of the motion platform as well as the size of the cutting tool, which could be a rotary cutter, laser, or EDM. For example, when using drilling for the inner diameter of a nozzle, the size is limited to the available drill bits. A summary of the

various materials, fabrication approaches, and nozzle characteristics for the traditional machining techniques are provided in Table 4. Images of the numerous traditionally machined MES nozzles are provided in Figure 7.

Previously Almekinders and Jones (1999) demonstrated a high-flow rate electrostatic spray approach using a serrated slot. This device was not operated in the cone-jet mode and exhibited poor droplet size distributions. Tang et al (2001) demonstrated a 9 nozzle array with a 30μm ID fabricated in polycarbonate using excimer laser machining. Bocanegra et al (2005) demonstrated a 37 nozzle array utilizing holes spaced 1-2mm instead of protruding nozzles. Duby et al (2006) demonstrated a single nozzle with 12 cone-jet sources anchored at slots machined using electrical discharge machining. Tran et al (2010) used traditional CNC milling to manufacture a 10 nozzle array on PMMA with a 300μm ID. Lhernould and Lambert (2011) used excimer laser machining to produce an 8 nozzle array with 150μm ID. Arnanthigo et al (2011) fabricated an 8 nozzle circular array from PEEK plastic with a 270 μm ID.

Table 4: Characteristic summary for traditionally machined MES nozzles

Year	Authors	Configuration	Nozzle Material	n	P	ID	L
1999	Almekinders and Jones	Linear serrations	Polymer				
2001	Tang et al	Square planar	PC	9	1.1mm	30µm	1mm
2002	Xiong et al	Square planar	Copper	81	~3mm	100um	
2005	Bocanegra et al	Hexagonal Planar	PEEK	37	1-2mm	500µm	~5mm
2006	Duby et al	Circular	Stainless Steel	12		1.2mm	
2010	Tran et al	Linear	PMMA	10	2-6mm	300µmx300µm	35cm
2011	Lhernould and Lambert	Linear	PC	8	2mm	150µm	750µm
2011	Arnanthigo et al	Circular	PEEK	8	13.8cm	270µm	1cm

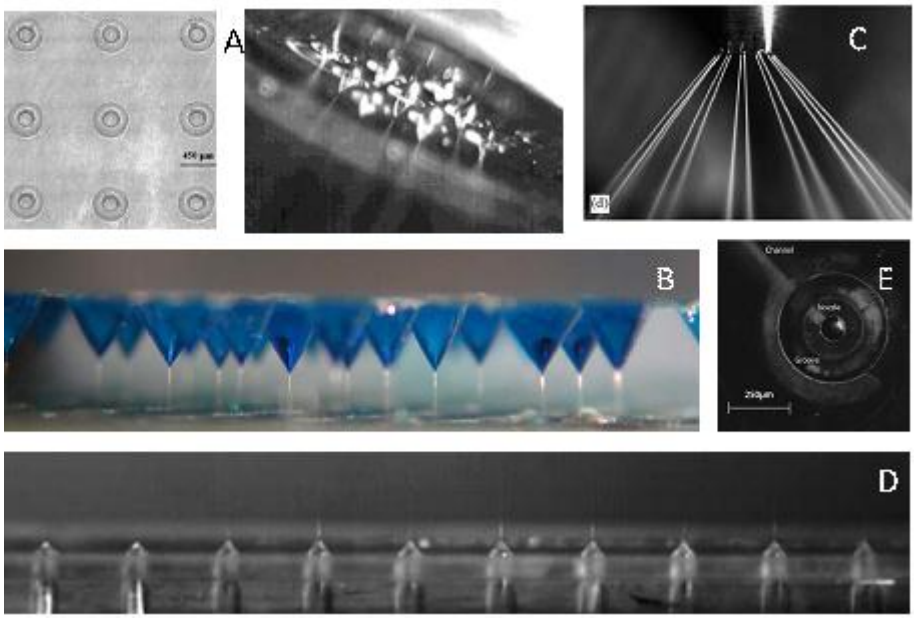

Figure 7: Images of traditionally machined MES nozzles. A - (Tang, Lin, et al. 2001), B - (Bocanegra, et al. 2006), C - (Duby, et al. 2006), D - (Tran, Byun and Nguyen, et al. 2010), E - (Lhernould and Lambert 2011)

1.5 Thesis Overview

After reviewing prior work on MES, CNC machining was chosen since it is a relatively straight forward, mechanical fabrication approach which offers great flexibility in terms of nozzle materials. Additionally prototyping is simplified since designs can be readily modified in CAD. CNC machining enables scalable and automated fabrication of MES arrays beyond the dimensions of silicon wafers and is limited only by the size of available CNC machines, which can be multiple meters. This paves the way to enabling electrospray as a wide area industrial coating tool in applications such as functional glass coatings where the manufacturing lines are many meters

wide. With CNC machining at the micron scale, we've achieved 20 source/cm linear electrospray arrays in aluminum, brass, and polycarbonate with 50μm and 100μm ID. We demonstrate that sub 100μm features can be reliably manufactured using conventional CNC drilling and milling machining techniques.

This work extends the literature of MES by inheriting the fundamental aspects of previous designs while focusing on the development of an approach which can be implemented in industrial manufacturing scenarios. Emphasis was placed on maintaining manufacturing technique scalability, developing new designs, and ensuring robust component integration. The work presented in this thesis is highly developmental and pragmatic by nature.

The rationale and analysis for the design and fabrication process of the system components are presented in chapter 2. Emphasis is placed on the functions of the distributor, extractor, and collector electrodes, as well as the integrator and other crucial components. The precision machining platform and procedures used to fabricate all components are highlighted.

In chapter 3, the design is analyzed in order to prescribe operating conditions and validate our numerical and analytical models. We applied the line-of-charge model to the linear array to obtain the spray profile model, which was then extended to determine the critical space charge field for the experiment. Photographs of the resulting spray cloud are compared to the spray profile model, showing good agreement. The average droplet size from each source in the array was characterized using Phase Doppler Interferometry, showing less than 3% relative standard deviation in droplet diameter across the array.

Chapter 4 investigates coating a TiO2 nanoparticle film onto silicon wafers using a 25 nozzle LINES device integrated with a heated and motion controlled stage. The speeds and driving field were varied and the resulting film morphology was studied using SEM, optical profilometry, and macro photography. The deposition patterns were compared with results from GPU simulation, showing good agreement in terms of the spray foot print and droplet number density flux.

We conclude in chapter 5 with conclusions and recommendations for improvement on future MES system designs, potential system configurations, and applications.

CHAPTER 2: SYSTEM DESIGN AND IMPLEMENTATION

This chapter presents an overview of the design rationale and fabrication approach for the MES device by breaking the entire system into three subsystems: the electrode, fluid, and integration subsystems. The primary design constraint of the device is maintaining equal electric and flow fields at each cone-jet site. The primary design goal is developing a robust system configuration from an industrial perspective, i.e. all components are mechanically rugged and can be disassembled, washed, and reassembled. This meant non-permanent schemes had to be developed for providing the fluid seal from the feed line to the distributor reservoir, electrical connections to the three electrodes, alignment of the distributor nozzles with the extractor opening, and a mechanical mount adaptable for various systems (i.e. PDI and thin film deposition). An overview of the fabrication technique for all components is also presented with an emphasis on the precision machining platform and process developed to manufacture the nozzle bearing distributor electrode.

2.1 Electrode Design

To enable cone-jet mode at high nozzle packing densities, previous successful MES devices utilized a 3 electrode configuration (Deng et al. 2007; Bocanegra et al. 2006). These 3 electrodes, named distributor, extractor, and collector, effectively separate the MES device into two isolated electric field regions, the cone-jet forming region and spray forming region (schematic is shown in Figure 8. A strong field, E_j, was applied in the jet forming region to establish and

anchor the cone-jets, and the driving field, E_d, was established in the spray region to guide the charged droplets towards the collector. The magnitude of the fields between them can easily be controlled by adjusting the three electrode potentials.

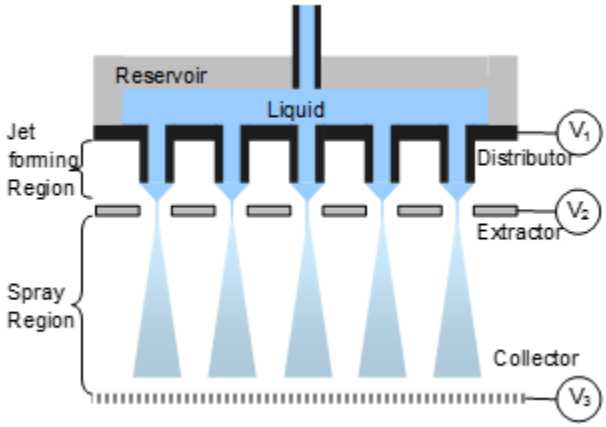

Figure 8: Diagram distributor-extractor-collector electrode configuration MES systems, effectively dividing the device into two electric field regions, the jet forming and spray forming regions.

A convenient configuration for MES utilizes two opposite polarity high voltage power supplies connected at the ground terminal. To operate in the positive ion mode, a positive power supply is applied at the distributor and a negative power supply at the collector with their ground leads connected at the extractor. For operating in the negative ion mode, the negative supply is connected to the distributor and positive at the collector, again with the grounds at the extractor. This gives a very simple way to control the electric field in each region by independently controlling the potential of the power supply connected at the distributor and collector. Alternatively, two of the same polarity power supplies can be used in by cascading the voltages appropriately so that the field always points in one direction for both the cone-jet and driving field regions. However in this configuration, both power supplies must be adjusted simultaneously to only adjust one driving field.

2.1.1 Distributor

The distributor is the nozzle containing electrode which initiates the spray by uniformly dividing the fluid flow to the nozzle tip where cone-jets form. Here the adopted electrode geometry at the distributor is a linear array of protruding cylindrical nozzles. To attain equal electric field, symmetry between the distributor nozzle tips and extractor opening is crucial. This symmetry is met by careful alignment during assembly. The nozzles on the array interior have neighboring nozzles that create a symmetric electric field for formation of cone-jets. At the edge of the array, there is only one neighboring nozzle. This creates an asymmetry in the electric field which repels the cone-jet away from the center of the array. This phenomenon is termed "edge effect," since the electric field is intrinsically stronger at the edge of the nozzle array and weakest at the center of the array. Emitters made from electrically conductive materials can still enhance the electric field at the edge by implementing dummy nozzles without microfluidic channels that create a mutual repulsion and minimize the edge effect. Such dummy nozzles are implemented here.

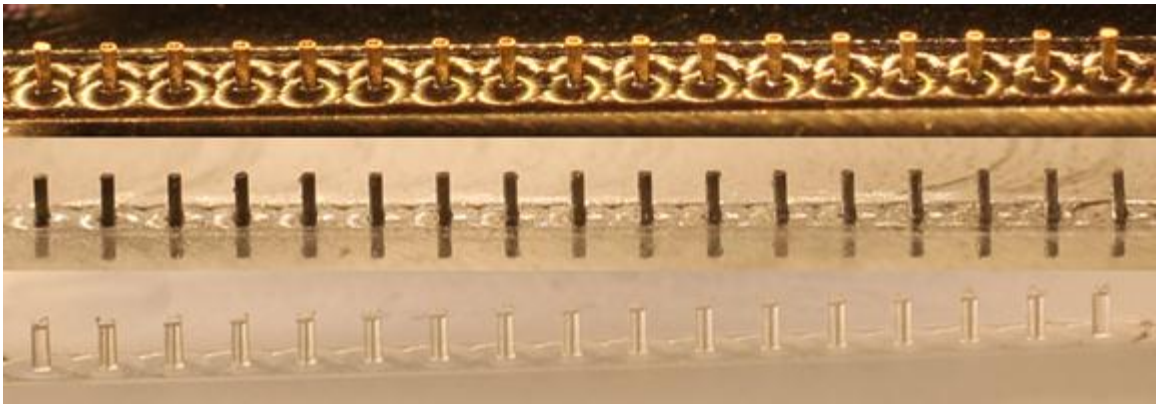

Figure 9: Linear MES arrays with ID = 0.05mm and P = 0.5mm machined in brass (top), aluminum (center), and polycarbonate (bottom)

2.1.1.1 Nozzle Microfluidics

Deng, Waits, and Gomez (2009) established a design rule to achieve approximately equal flow fields for all nozzles: the viscous pressure drop through the channel, given by the Hagen-Poiseuille Equation, must be comparable to the electrohydrodynamic pulling pressure, which is comparable to the Laplace surface tension pressure at the nozzle tip. Using the parameters of the experimental setup, it can be seen that the design rule in given by Equation 1 has been satisfied, where ethanol viscosity and surface tension ($\mu = 1.07\text{x}10^{-3}$ Ns/m^2, $\gamma = 2.23\text{x}10^{-2}$N/m), microchannel length, inner diameter, outer diameter, and flow rate ($L = 5\text{x}10^{-4}$m, $ID = 5\text{x}10^{-5}$m, $OD = 1.2\text{x}10^{-4}$m $Q=1.39\text{x}10^{-10}$m^3/s).

$$\frac{128\mu LQ}{\pi ID^4} \approx \frac{4\gamma}{OD} \Rightarrow 487 \approx 742 \quad (1)$$

2.1.2 Extractor

The extractor is an electrostatic barrier electrode between the distributor and collector that protects the vulnerable cone-jet forming region from the space charge created by droplets in the spray region. The extractor is usually a plate that is directly downstream from the distributor with an opening aligned to the nozzles. The opening allows the droplets generated in the cone-jet forming region to pass through to the spray forming region immediately after jet breakup. The opening on the plate may be individual holes corresponding to each nozzle or a slot aligned to a linear row of nozzles. Other extractor configurations have been implemented including ring and

rod electrodes. Here we implement a slot extractor, which was adopted over hole geometry since the device is less prone to flooding, alignment becomes simpler, and electric field isolation is sufficient.

Figure 10: Extractor machined in aluminum with a 0.5mm slot

2.1.2.1 Electric Field Simulation

To verify the effectiveness of the electric field generated by a slot extractor as opposed to a traditional hole extractor, both electrode designs were simulated using COMSOL Multiphysics. To model the nozzle geometry, cylinders with the same height and outer diameter as the nozzles in the 51 nozzle device were used. Spherical caps were superimposed at the tip of the cylinders to simulate a conductive liquid meniscus. Two simulations were performed using extractors spaced 375 μm away from the tip of the nozzles. One used an extractor with 500 μm diameter holes and another with a slot of 500 μm opening width. The boundary condition at the extractor surface was ground potential and high potential at the nozzle surface. The simulation results presented in Figure 11 show that nozzles at potential of 1.2kV using a hole extractor produces almost identical electric field as those nozzles at 1.3kV using a slot extractor. The modest increase in required voltage for

slot configuration is acceptable because the slot extractor brings the benefits of alignment ease and higher tolerance to accidental flooding without exceeding the breakdown threshold.

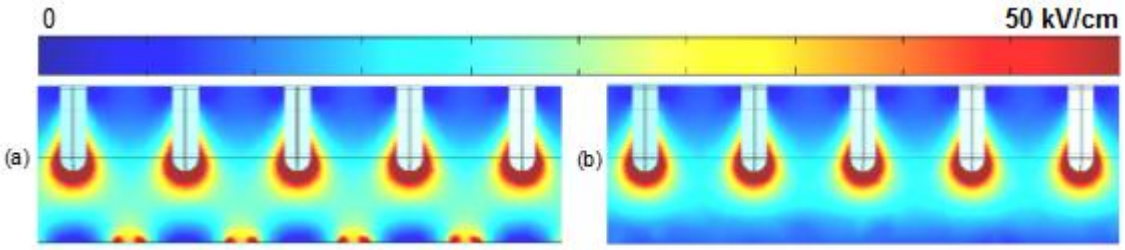

Figure 11: Electric field simulation comparing the hole (a) and slot (b) extractor designs.

2.1.3 Distributor-Extractor Spacer

A polycarbonate film spacer was fixed between the distributor and extractor to electrically insulate the electrodes and precisely space the nozzle tip and extractor slot. The film was fixed by the extractor mounting hardware and kept the extractor and distributor in intimate contact. Films of specified thicknesses are readily available down to 125±12.5µm in 125µm increments. By installing a different film thickness, the spacing can be easily modified. 375µm and 500µm film sections cut into small 1.5x1.5cm squares were used. During assembly, the squares were set into place and secured by the extractor after tightening the hardware. In the first generation LINES device, the extractor hardware was used to secure the spacer, align the distributor and extractor, and also provide the clamping force for the gasket fluid seal. This was later modified by adding an extra set of hardware at the distributor to seal the gasket and decoupling the fluid seal with the extractor alignment and spacer.

2.1.4 Collector

The collector is the electrode furthest downstream where droplets are collected after traveling through the spray region. Two different collector geometries were used in this work, a flat plate and cylinder. In both cases, the extractor to collector distance remained 1-5cm. This spacing provided sufficient driving field strength (~2-10kV/cm) to overcome space charge using a 10kV power supply. The cylinder collector was used for PDI measurements, and the flat plate collector was used for TiO_2 nanoparticle deposition.

2.2 Integration

The distributor must be integrated with other components to feed the liquid, connect to the power supply, properly align the extractor, and mechanically mount the assembly. In this section we discuss how these challenges were met.

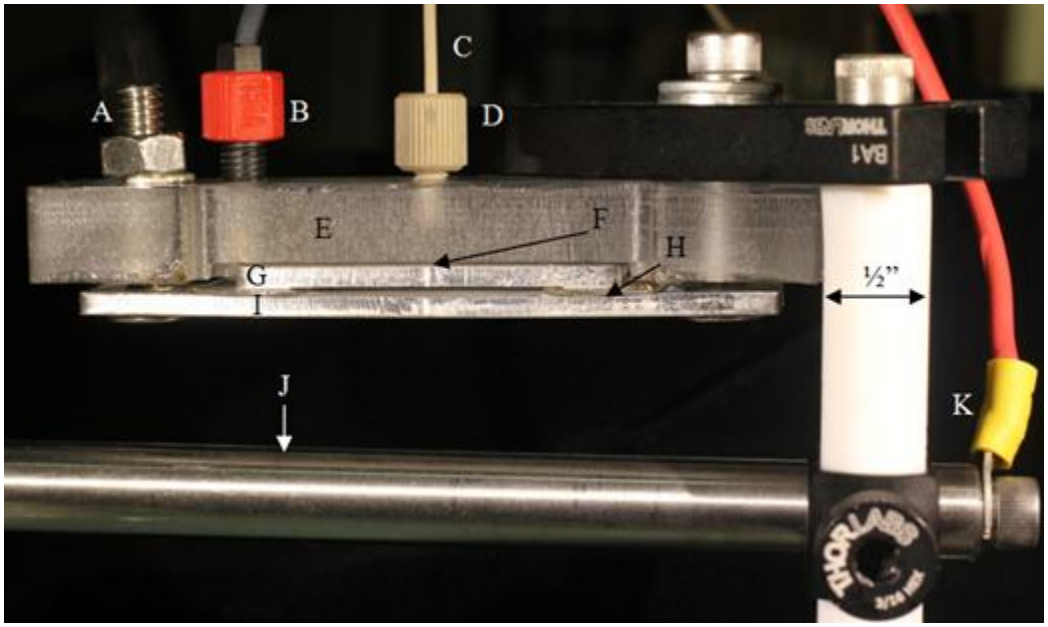

Figure 12: Image of the integrated MES system: A – Extractor electrical connection, B - Distributor electrical connection, C –Fluid line, D – Fluid fitting, E – Integrator, F – Gasket, G – Distributor, H- Spacer, I- Extractor, J- Collector, K- Collector electrical connection

2.2.1 Integrator

The integrator is a crucial component that was designed in this work to provide means for fluid, electrical, and mechanical connections at the distributor and extractor. The integrator is a rectangular component measuring 4"x1"x½", and was machined from ½" thick polycarbonate since it is inexpensive and resilient against ethanol. There are three main features on the integrator; fluid inlet, electrode contacts, and mechanical mount. The fluid inlet is in the center of the integrator and is a tapped hole (either 10-32 or ¼"-28) for the ferrule fluidic connector extending

halfway through the thickness. From the halfway point, a 1/16” diameter thru-hole extends so fluid can flow through. The tapped hole only extended halfway to provide a bottoming surface for the ferrule fitting to tighten onto the feed-line. On the opposite side of the fluid inlet, there is a recess which provides a constraint for the o-ring to keep it centered. At the corner of this recess there is a ¼”-28 thru-hole for the electrical connection to the distributor. The connection was done in the corner since either the reservoir or o-ring covers the area in the middle. Two ¼”-20 tapped thru-holes are centered on each side of the recess. The extractor, spacers, distributor, and o-ring are all aligned under a microscope and secured by using two ¼”-20 countersunk screws. Moreover, these holes provide means of electrical connection to the extractor.

2.2.2 Electrical Connections

Secure, yet removable electrical connections were made at the distributor, extractor, and collector. This overcomes limitations of glued, taped, or alligator clipped connections used in previous devices. The distributor and extractor electrical connections were secured using threaded connections at the back of the integrator. Besides providing a secure connection for a fluid line, it was realized that the hollow inner structure of microfluidic fittings provide a convenient thru hole for an electrical wire. With this in mind, a custom ferrule electrode was fabricated. Brass was chosen as the material so the ferrule could be soldered, as most non-cuprous metals cannot be soldered, e.g. aluminum. A ¼”-28 fluidic fitting was slid over the high voltage wire rated to 10kV and the ferrule electrode was soldered to the tip of the wire. This ferrule electrode could be threaded

into the ¼”-28 thru hole on the backside of the integrator and tightened in place once in contact with the distributor. Moreover, this design is safe since it the electrode remains well hidden. To connect the extractor, ground leads from both power supplies were joined and soldered into a ring terminal. The two countersunk ¼”-20 screws holding the integrator assembly together are in intimate contact with the extractor but insulated from the distributor by the polycarbonate spacers. These screws only extend about halfway through the thru holes so a ¼”-20 set screw was insert from the back side and tightened until it contacted the countersunk screw. The ring terminal connected to the power supply grounds was slid over set screws and secured by tightening a nut on top. In a similar manner, a ring terminal was connected to the high voltage output of the collector power supply. Since the cylindrical collector was a standard ½” stainless steel optical hardware post, the ring terminal was simply fixed with a ¼”-20 bolt on the end.

2.2.3 Fluid Connections

Pure ethanol was delivered from a 20ml syringe via New Era Syringe Pump systems Inc. Model NE-300 syringe pump. To connect the syringe pump to the integrator, a PEEK tube with 1/16” outer diameter and 1mm inner diameter was used as a feed line. A luer to 10-32 thread adapter was used in conjunction with a 10-32 PEEK microfluidic ferrule fitting to provide a leak proof seal from the syringe to feed line. The feed line was then secured to the back of the integrator at the fluid inlet via ferrule fitting. Incorporating a design using a feed line will allow other types of pumping systems besides a syringe pump to be used in the future.

We adopted an o-ring to provide a leak-proof, non-permanent seal between the integrator and distributor. We cast a custom oval shaped o-ring about to fit the rectangular collector. Sylgard PDMS was cast into a precision machined aluminum mold, heated at 60^{o}C for 30 minutes and then 90^{o}C for another 30 minutes. After cooling, the o-ring was carefully removed from mold. The final o-ring thickness was about 0.4mm. Designing and fabricating the o-ring enabled a tailored flat o-ring design for the integrator-distributor seal.

2.3 Fabrication

Prototyping and fabricating high density MES devices is prerequisite to any experiments. In order to eliminate the complexity and decrease the cost associated with silicon microfabrication, a precision machining process was developed in our lab specifically for MES fabrication. We implemented two 3-axis machining platforms in this work, one precision machining system with 1μm resolution and one macro-machining setup with 20μm resolution.

2.3.1 CNC Machining Process Flow

To prototype devices in our lab, we first designed 3D CAD models of components using SolidWorks 2009. The machine tool paths were then generated using CAMWorks, an automated manufacturing package which runs within the SolidWorks environment. The tool geometry,

machining speeds, and cutting strategies must be defined to generate a tool path. The tool paths were exported as machine readable g-code and executed using EMC2. The process was repeated to change tools, e.g. drills, and endmills, and run different paths until the part was completed.

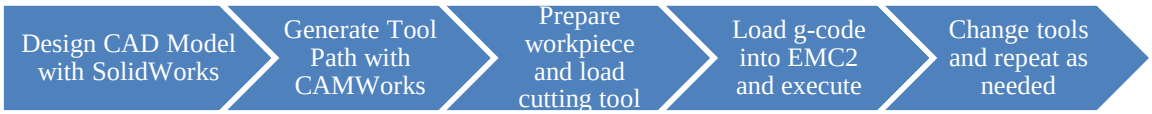

Figure 13: Machining process flow

A constraint of traditional machining is that internal features such as holes or slots depend on the tool geometry. Yet, commercial tungsten carbide drills and endmills are available in the micron and even nanometer size range with aspect ratios up to 10:1. The 50μm inner diameter of the nozzles used in the LINES device set a constraint on the micro-channel length L = 500μm. For arrays spanning far beyond this length, such as LINES at 25mm, there is a requirement to have enough mechanical rigidity for handling during assembly or cleaning and for an effective fluidic seal. To address this, a 1mm wide slot reservoir was machined on the back, effectively thinning the device down to 475 μm locally at the nozzle area to allow the drill through. We found that this slot reservoir did not affect the device performance.

2.3.2 Macro-Machining

To manufacture custom components that do not require high tolerance precision machining, we implemented a 3-axis desktop CNC, model CNC2520 from CNCDIY, with 20μm resolution with a 200mmx250mmx50mm (XYZ) working table. The system is equipped with a spindle capable of 12,000RPM and a 1/8" collet and can be used to machine wood, plastic, and soft metals such as aluminum and brass. We used this system to machine the integrator and extractor. Initially we tried to machine distributors on this system but found that the accuracy of leadscrew assembly was too poor for handling micron level tolerances. Moreover, the spindle suffers from runout of about 50μm and small cutters with diameters below 250μm cannot be used since they break upon first cut.

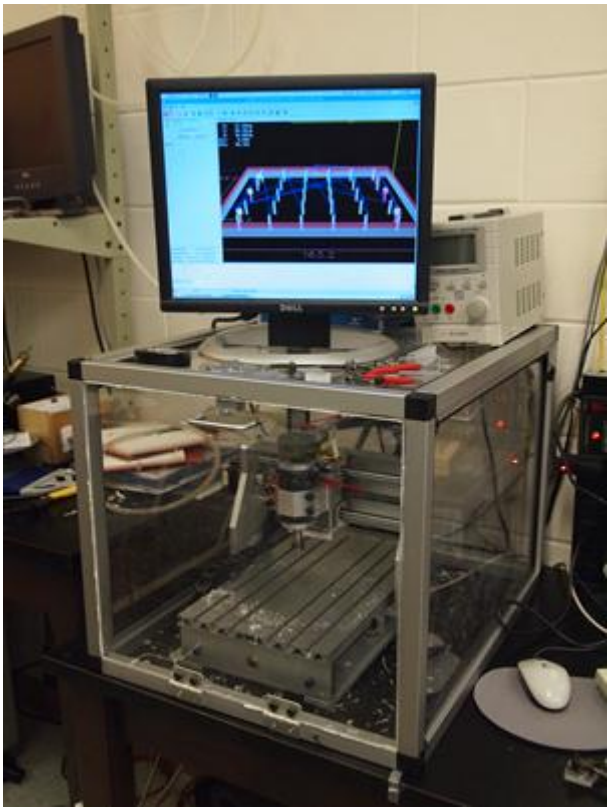

Figure 14: CNCDIY – 2520 Macro-machining setup

2.3.3 Precision Machining

To meet the precision machining demands of the micron sized nozzles on a budget constraint, we assembled our own 3 axis precision CNC machine. Three Newport TS-series linear stages (previously used in a stereolithography system developed in our lab before we were tenants), were assembled into an XYZ configuration. A NSK precision high-speed spindle capable of 25,000 RPMs with 5 µm runout was mounted onto the platform. 50 µm diameter microdrills and

250 μm and diameter endmills (Kyocera microtool) were used to machine the inner and outer nozzle diameters respectively. To prevent breakage and provide lubrication and cooling of the microdrills, ethanol was fed over the drilling area of each hole. The ethanol flow effectively removes the chips produced during drilling from the hole and drill flutes. If the chips build up in the flutes of a microdrill, it will break after drilling only a few microns.

Initially the stock controller for these stages (Newport ESP6000) was used, but was found to be unable to produce the needed accuracy for machined parts. The TS-Series stages used servo motors and 0.5um resolution optical encoders and was controlled using a PID algorithm and while traversing the tiny radius around the nozzles, a large centrifugal acceleration is demanded from the system which caused out-of sync motion and irregularities in the nozzle shape. Moreover, the interface for the ESP6000 controller did not support g-code and machine paths had to be mapped by hand and input line by line. This process was highly error prone and very tedious. To overcome these limitations, the stages were retrofit with 10:1 stepper motors to enable control using a generic TB6560 stepper driver board commanded by EMC2. This approach ended up proving successful in both producing more circular, concentric nozzles and enabled g-code input. The encoders were also retrofit to input into EMC2 which gave verification of the accuracy in commanded motion. The smallest incremental motion with the stepper motors was 0.25μm. Using this system, nozzle arrays were fabricated containing between 1 to 101 nozzles in brass, aluminum, polycarbonate, Teflon, and acrylic. The brass, aluminum, and polycarbonate nozzle arrays are featured in Figure 9.

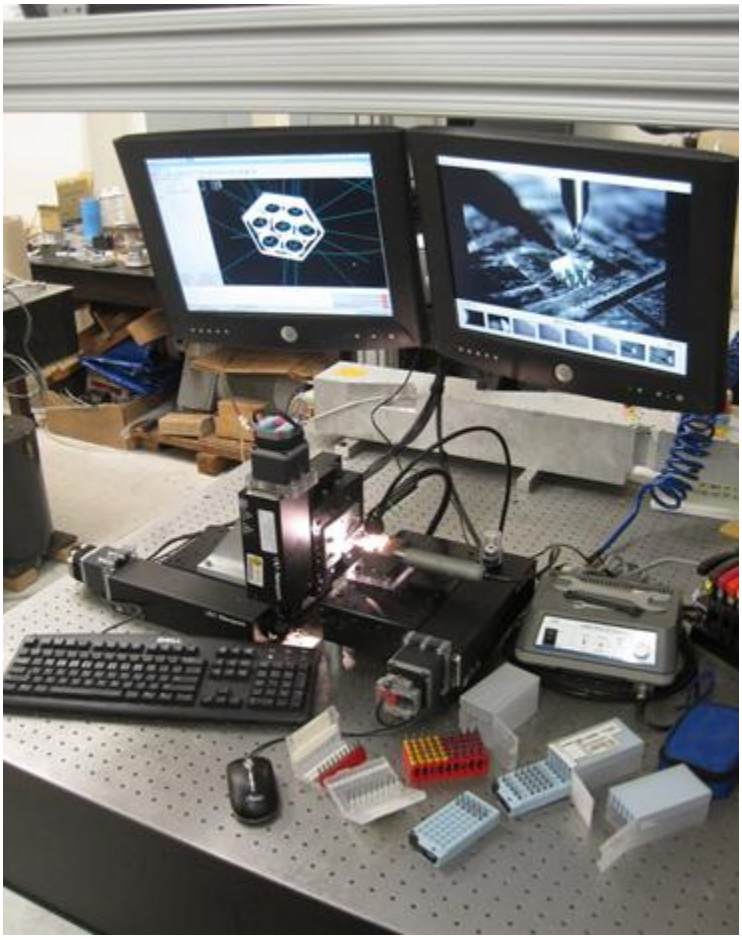

Figure 15: Precision micro-machining setup

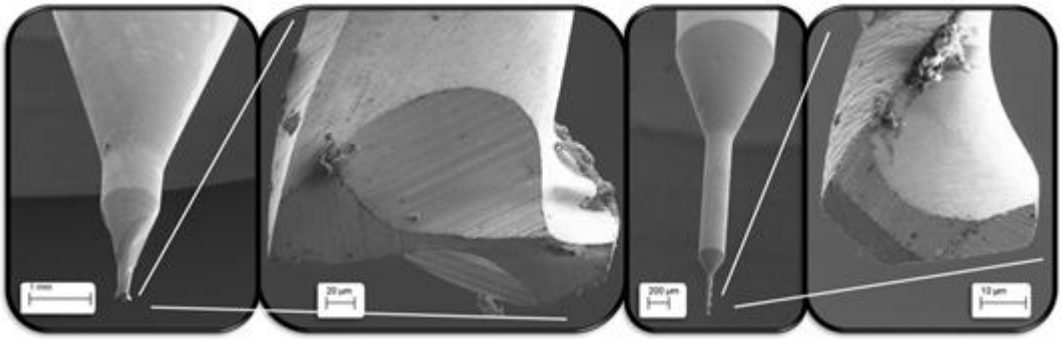

Figure 16: SEM images of micro-tools, 250µm endmill (left) and 50µm drill (right)

2.3.4 Distributor Machining Post-Treatment

After machining nozzles, a post treatment was performed by etching the part in a bath of in a 20:1 ethanol:HCl solution for 1 minute. This assisted removal of any remaining burrs which that cause irregularities in the electric and or flow fields. After treatment, the components were submerged in a bath of ethanol to terminate etching, ultrasonically cleaned, and dried with filtered compressed air prior to assembly.

CHAPTER 3: SYSTEM OPERATION AND SPRAY CHARACTERIZATION

In this chapter, a methodology for prescribing the working extractor-collector driving field is estimated and described based on the requirement that the critical space charge field generated by the spray cloud must be overcome. The line-of-charge model is extended to estimate the approximate spray profile and the critical space charge field, which is then used to prescribe the operating conditions for a 51 nozzle LINES device (P=0.5mm, ID=50μm, L=0.48mm). The LINES device is then integrated with a 3-axis micrometer stage and Phase Doppler Interferometer (PDI) to measure the average droplet size across the array, which demonstrated <3% RSD across all 51 nozzles. Finally, the resulting experimental spray profile is compared with the spray profile model and a numerical simulation spray profile.

3.1 Operating Requirements

To ensure robust operation of the linear electrospray array, the droplet fly-back must be mitigated; otherwise droplets will accumulate and eventually flood the extractor, inhibiting operation (Deng and Gomez, 2007). The droplet fly-back, sometimes referred to as satellite trapping, occurs due to the repulsive field generated by the intense space charge of the dense cloud of charged droplets. As discussed in Section 2.1.2, the extractor electrode serves as the barrier between the cone-jet forming region and spray cloud region to establish two separate electric fields. However, the potential required at the extractor and collector must be carefully determined

to ensure the extractor serves its purpose to sufficiently accelerate all of the droplets toward the collector. To avoid droplet fly-back, the minimum required extractor-collector potential will establish an electric field of magnitude greater than the largest space charge electric field; the driving field E_d applied between the extractor and collector must exceed a critical value E_c.

For an electrospray, the space charge field is most intense right after jet breakup near the extractor. For an array of electrosprays, it is similarly also near the extractor, but relative to the nozzle array, it is most intense and at the center of the nozzle array. As the spray naturally expands due to Coulombic repulsion, the charge density decreases. The charge density of an array is dependent upon the current emitted from each nozzle and the geometric layout of the nozzles. In order to quantify this crucial electric field, we generalized the problem using an approximate spray profile model.

3.1.1 Approximate Spray Profile Model

We previously derived a spray profile model to describe how the spray cloud from a source of linear nozzles expands along the *x* and *y* directions (Yang et al., 2012). Figure 17 shows a schematic of the coordinate system used to model the spray profile of LINES. The following assumptions are applied to simplify the problem: i) the spray consists of monodisperse, mutually charged droplets with negligible inertia; droplet motion is dictated by $\vec{V} = Z\vec{E}$, where Z is the mobility of the droplet, $\vec{V}$ is the droplet velocity, and $\vec{E}$ is the electric field, ii) constant axial

droplet velocity, u (Deng and Gomez, 2007), iii) volumetric charge density ρ does not vary along the x-direction; $\partial\rho/\partial x = 0$, iv) The x component of the space charge field, $\vec{E}_\rho$, is negligible compared to the magnitude of the driving field $\vec{E}_d$ (Deng and Gomez, 2007).

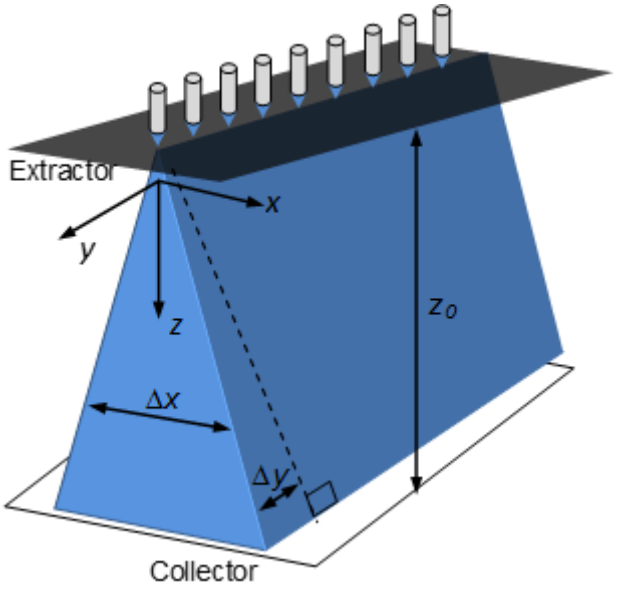

Figure 17: Model and coordinate system for the linear MES array spray profile model

By combining these assumptions with the law of charge conservation and Gauss's law, at steady state, we reach solution for the charge density as a function of the droplet velocity, z-position, and mobility, given by:

$$\frac{1}{\rho} - \frac{1}{\rho_0} = \frac{Z}{\varepsilon_0 u} z \tag{2}$$

where $\rho_0=\rho(z=0)$, or at the exit of the extractor. Immediately after cone-jet breakup, the droplets are linearly aligned, thus making ρ_0 very large, and $1/\rho_0$ negligible compared to $1/\rho$. If we assume

the spray does not expand significantly along the *y* direction, we can arrive at an expression for the charge density by dividing the net current (single nozzle current multiplied by the number of nozzles) by the spray flow rate (droplet velocity multiplied by the area) as:

$$\rho = NI_0 /(NP_0 \cdot 2x \cdot u) = I_0 /(2P_0 xu) \tag{3}$$

where P_0 is the distance between two neighboring nozzles. Since $u = E_d \cdot Z,$ by plugging *u* into Eq. (2), we arrive at the result for the *x*-direction spray profile width as a function of *z*:

$$\Delta x = \frac{I_0}{2P_0 \varepsilon_0 Z E_d{}^2} z \tag{4}$$

This equation suggests that the projection of spray on *x*-*z* plane resembles an isosceles triangle with the apex angle determined by the coefficient on the *z* term. This leads to the conclusion that an increase in the nozzle pitch or droplet mobility will lead to a linear decrease in the apex angle, while the driving field will quadratically decrease the apex angle. Similarly, an increase in the current will lead to a linear increase in the apex angle.

The *y*-expansion is primarily determined by the spray axis bending, caused by the repelling force exerted by other sprays (Snarski & Dunn 1991). By approximating the spray as a line-of-charge (Deng and Gomez, 2007), we can treat axis bending of the spray at the edge as the result of E_y, which is the radial component of the electric field introduced by all other line-of-charge when N is sufficiently large:

$$E_y = \frac{\lambda}{2\pi P_0 \varepsilon_0} \sum_{i=1}^{N-1} \frac{1}{i} \approx \frac{I_0}{2\pi P_0 \varepsilon_0 u} \ln(N) \tag{5}$$

Here λ is the line charge density $\lambda = I_0 / u$.

The spray axis separation velocity is:

$$u_y = \frac{dy}{dt} = E_y Z = \frac{I_0 \ln(N) Z}{2\pi P_0 \varepsilon_0 u} \tag{6}$$

The solution to Eq. (5) is:

$$\Delta y = \frac{I_0 \ln(N)}{2\pi P_0 \varepsilon_0 Z E_d^{\,2}} z \quad . \tag{7}$$

Very similar to Eq. (3), Eq. (6) suggests that the projection of spray on *y*-*z* plane resembles an isosceles trapezoid; essentially the same profile as the *x*-*z* plane, but split in half with a long rectangle in the middle due to the linear array along this direction. This might suggest a constant NP_0 be added to Eq. (6) to account for this rectangle in the center of the array, since Δy only captures the expansion from the edge of the nozzle array. Eq. (6) also leads to the conclusion that an increase in the nozzle pitch or droplet mobility will lead to a linear decrease in the apex angle, while the driving field will decrease the apex angle quadratically. Similarly, an increase in the current will lead to a linear increase in the apex angle. Moreover, for N=51, P_0=0.5mm, the typical value of Δy is 1.7mm, which is insignificant compared to the value of original total spray width (NP_0= 26 mm). With the constant correction, the spray width becomes 27.6 mm, which is very close to the measured width of 27.5 mm.

3.1.2 Prescribing Operating Conditions

The same line-of-charge approximation used to obtain the spray profiles is extended to estimate the critical electric field value, E_c, which is equal to the maximum space charge field that appears in the "critical zone" located at close proximity to the center of the spray immediately after the spray passes through the extractor (x~0, z~0). Note that the center spray is the considered as the 0th spray (assuming an odd number of nozzles) while the i^{th} pair includes the two sprays at a distance iP_0 from the center. The z component field $E_{c,i}$ near the "critical zone" caused by the i^{th} group is given by:

$$E_{c,i} = 2\int_0^{z_0} \frac{\lambda z}{2\pi\varepsilon_0((iP_0)^2 + z^2)^{3/2}} dz = \frac{\lambda / \pi\varepsilon_0}{\sqrt{(iP_0)^2 + z^2}} \Bigg|_0^{z_0} = E_{ref} \frac{1}{i}\left(1 - \frac{1}{\sqrt{\alpha^2 / i^2 + 1}}\right) \tag{8}$$

where $E_{ref} = \lambda/(\pi\varepsilon_0 P_0)$ and $\alpha = z_0/P_0$. Because typically z_0~10mm, and P_0~0.5mm, α is on the order of 10. Since $E_{c,i} < E_{ref}/i$, we can estimate the upper limit of the critical field:

$$E_c = \sum_{i=1}^{(N-1)/2} E_{c,i} < \sum_{i=1}^{(N-1)/2} E_{ref} \frac{1}{i} \approx E_{ref} \ln(N/2) \tag{9}$$

Using the values for line charge density λ = 2×10^{-9}C/m, P_0 = 0.5mm, and N = 51, yields E_c = 4.3 kV/cm. This value was used to prescribe the extractor-collector distance and collector potential. A rough estimate of the E_d was calculated as $E_d = V_c/z_o$; the extractor-collector potential difference, V_c, over the extractor-collector distance, z_o. Since the maximum possible voltage of the collector power supply is 10kV, an extractor-collector distance of 1.5cm was chosen to give

headroom for increasing E_d slightly beyond E_c so that the effect of modifying E_d could be studied without inhibiting operation of the system.

When the critical driving field value is plugged into Eq. (7), the resulting spray profile can be considered to give the maximum width for sustaining spray operation. If the field decreases, droplet fly-back will flood the extractor and the spray will cease. Therefore, since the driving field can only be equal to or greater than this field, the spray profile width can only be decreased from the critical field width.

Before ending this section, we summarize the limitations of the spray profile model. The spray profile model is intended to provide a quick way to estimate how the spray evolves. For this purpose, we have dramatically simplified the problem after making many assumptions. In the spray profile model, we neglected the satellite droplets, and did not consider the droplet evaporation and fission. We also assumed the droplets reach terminal velocity instantaneously due to the low Reynolds number. The driving field is assumed to be intense enough to prevent satellite droplet fly-back (Deng and Gomez, 2007). The spray profile model is based on parallel flat electrodes (extractor and collector), instead of the needle-to-plate configuration, which introduces radial component of the electric field. It is important to keep these simplifications and assumptions in mind therefore we can apply the spray profile model properly without introducing significant errors.

3.2 Spray Profile

The spray profile model was compared against experiment to verify its validity. A numerical simulation was also used to model the interactions of droplets from MES devices. A 51 nozzle LINES device (P=0.5mm, ID=50μm, L=0.48mm) fabricated in aluminum was used to experimentally verify the results from the spray profile model and a numerical simulation. The LINES device was sprayed at 0.5 ml/hr/nozzle (25.5ml/hr total) and imaged using a Canon Rebel T2i with a Sigma 50mm f/2.8 Macro lens. The camera was set to a long enough exposure time so that streak lines from the droplet trajectories were recorded. The spray plume was illuminated using a laser sheet created by sending a laser beam through a cylindrical prism.

A numerical simulation was developed to study the interactions of electrosprayed droplets from multiplexed arrays (Yang et al., 2012) using a Lagrangian method (Ganan-Calvo et al 1994; Wilhelm et al 2003, Deng et al, 2007; Oh et al. 2008). The Lagrangian model tracks each droplet's motion. We used graphics processing units (GPUs) to handle the heavy computational load and model the forces of drag from the surrounding gas, electrostatic repulsion amongst droplets, driving field, and the image force.

Images of the x-z plane of the spray profile produced in the GPU simulation, experiment, and spray profile model can be seen in Figure 18. Images of the y-z plane produced in the GPU simulation and experiment can be seen in Figure 19. The results produced are quite consistent among each of the techniques used, which verifies the soundness of the assumptions made within the derivation of the model. It also verifies that the numerical model captures and emulates the physics of the forces amongst interacting electrosprayed droplets. The top portion of the

experiment images are blocked from sight due to the extractor. The reflection of the laser beam off of the extractor and other surfaces in close proximity create a glare and streak effect in the image, but does not degrade the ability to compare it with the simulation.

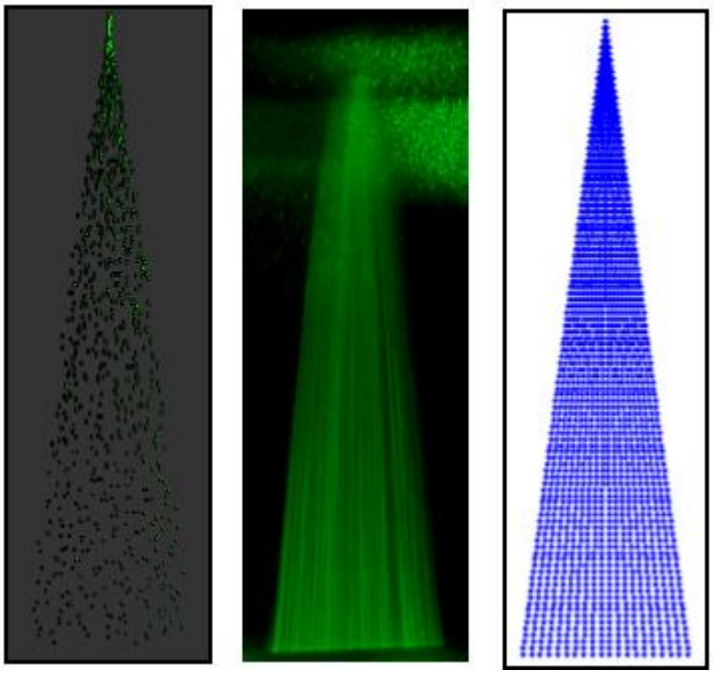

Figure 18: Comparison of the x-z plane spray profile from GPU simulation (left), experiment (center), and spray profile model (right)

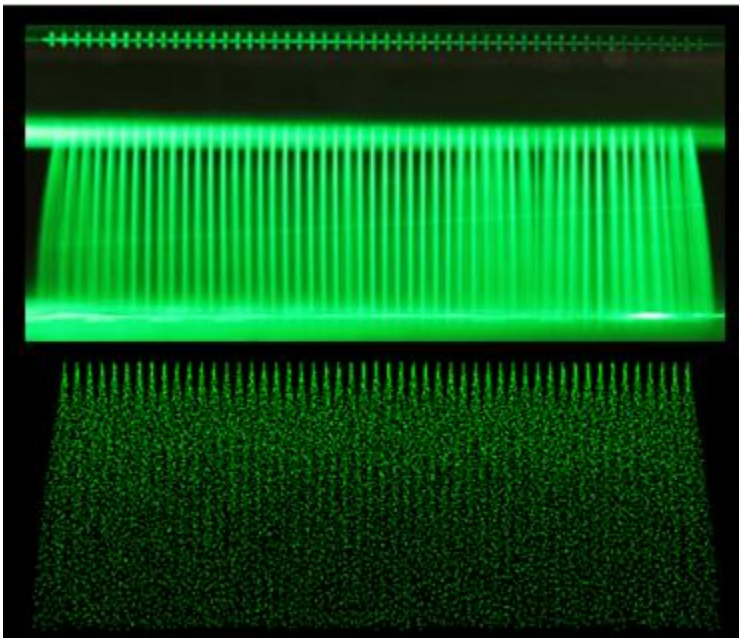

Figure 19: Comparison of y-z plane spray profile from experiment (top) and GPU simulation (bottom)

3.3 Droplet Size Distribution

The droplet size emitted from each nozzle across the 51 nozzle array was measured using Phase Doppler Interferometry (Artium). The average droplet diameter remained uniform across the array and exhibited the largest relative standard deviation at the lowest flow rate measured.

3.3.1 PDI Principle

Phase Doppler Interferometry is a non-intrusive, laser based diagnostic technique for measuring droplet size and velocity. In 1980, Bachlo (Artium's founder) theoretically described light scattering from spherical particles and showed that the phase shift of the light scattered from two intersecting beams could reliably measure the diameter of spherical particles. The technique has since evolved as the standard laser-based diagnostic instrument for simultaneously measuring the size and velocity of individual spherical particles. In this work, we were fortunate to come into the market 32 years after the PDI's inception, and had the ability to purchase an advanced 'self contained' PDI. A self contained unit is essentially a single box which houses all of the optic components, e.g. lenses, prisms, filters, mirrors, lasers, photodetectors, etc. Heritage PDI systems require manual setup and alignment of all of these components on an optical table, which can consume a considerable amount of time to setup and maintain. Refer to Figure 20 for a schematic of typical PDI system components.

In summary, the PDI uses a monochrome laser (diode pumped solid-state 532nm) in conjunction with a beam splitter to divide the initial laser beam into two beams of equal intensity and wavelength. These two beams are then sent through a series of lenses and mirrors and out of a window at an approximate 7° angle. The beams then intersect at the probe volume, where a fringe pattern will appear due to the interference of the two beams. The fringe spacing is proportional to the laser wavelength over the sine of the beam intersection angle. The well-defined fringe pattern becomes the basis for interrogating droplets.

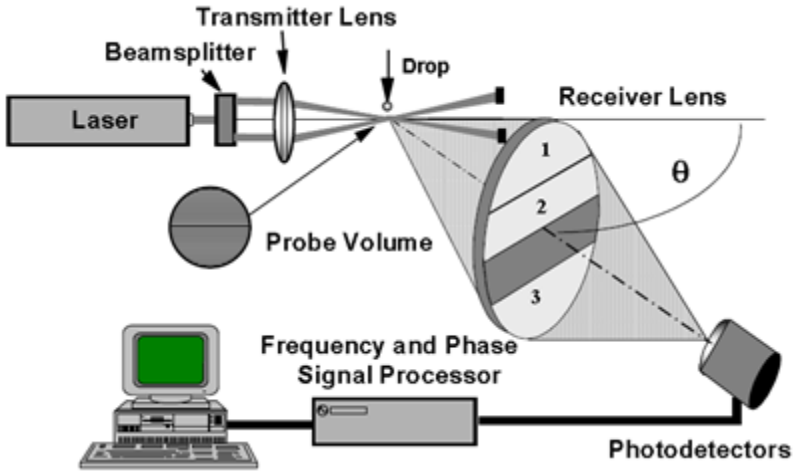

Figure 20: PDI system components

Droplets are then brought to pass through the probe volume with some velocity. Each droplet acts like a lens, refracting the incident light at an angle dependent upon its curvature, i.e. its diameter. More specifically, the passing droplets refract and magnify the interference fringes in the probe volume. Smaller droplets with larger curvature diverge and magnify the fringes more than large droplets with intrinsically smaller curvature. The refracted fringe pattern is then collected by a series of photodetectors placed at calibrated spacing. For a single droplet, the signals on each photodetector are identical in frequency and amplitude, but with a slight shift in the signal's time signature (phase) due to the distance between photodetectors. This phase shift is proportional to the size of the droplet, while the signal's frequency is used to derive the droplet velocity.

3.3.2 System Setup

The same 51 nozzle LINES devices described in 3.1.2 was integrated with a 3-axis micrometer stage and mounted near the probe volume of the PDI. The micrometer stage enables the ability to scan the linear array across the PDI, and probe specific points within the spray cloud emanating from individual nozzles, e.g. near the edge of the spray plume, near the distributor, near the extractor, etc. The device was operated with all nozzles spraying in the cone-jet mode as verified by a Canon Rebel T2i camera with a Sigma f/2.8 50mm macro lens at 10x digital zoom. A Stanford Research Systems, Inc. PS350 high voltage power supply was used at the distributor, capable of up to 5kV at 5mA. A Tianjin Dongwen High Voltage Power Supply Co., Ltd. high voltage power supply was used at the collector, capable of supplying -10kV at 1mA. Pure ethanol was delivered from a 20ml syringe via New Era Syringe Pump systems Inc. Model NE-300.

3.3.3 Results

The measured droplet sizes were plotted against the nozzle number for the three flow rates 15.3, 25.5, and 35.7 ml/hr (0.3, 0.5, and 0.7 ml/hr/nozzle). The D_{10} average droplet diameter from each nozzle was measured by taking 2,000 droplet measurements at each point, which took approximately 3-5 seconds of data collection before moving to the next measurement point. The average droplet diameter and relative standard deviation across the array are summarized in presented in Table 5.

Table 5: Summary of PDI measurements statistics for the 51 Nozzle LINES device

Flow Rate (ml/hr/nozzle)	0.3	0.5	0.7
Average Droplet Diameter (µm)	7.18	9.25	12.0
Relative Standard Deviation	2.66%	1.79%	1.89%

The typical scaling of droplet size with flow rate can also be seen as the average droplet diameter across the array increases from 7.18-12.0µm as the flow rate per nozzle increases from 0.3 to 0.7 ml/hr. The results from the PDI data also validate the fluidic design rule, showing that relatively equal flow rates are achieved from source to source. Although the total flow rate through the device is known by programming the syringe pump to a set value, obtaining a direct measurement of flow rate through individual nozzles is simply impractical. But, since droplet diameter is dependent upon flow rate, we can effectively measure the flow rate through each nozzle by measuring the droplet diameter. As seen in Figure 21 the low deviation in droplet diameter across the array shows that the flow rate through individual nozzles also has a low deviation, empirically validating the fluidic design rule discussed in 2.1.1.1 .

During acquisition of the PDI data, the flow through each nozzle would sometimes become partially blocked by debris, and the flow rate would consequently decrease. This was verified by a decrease in the average droplet diameter in the PDI measurement and visual inspection of the spray cloud, showing greater expansion in the x-z plane and weaker refracted light intensity. Therefore, the device sometimes required purging, a firm tap, or disassembly and rinsing to remove the clog and achieve uniform flow again. A filter for the liquid prior to flow into the reservoir would help prevent clogging.

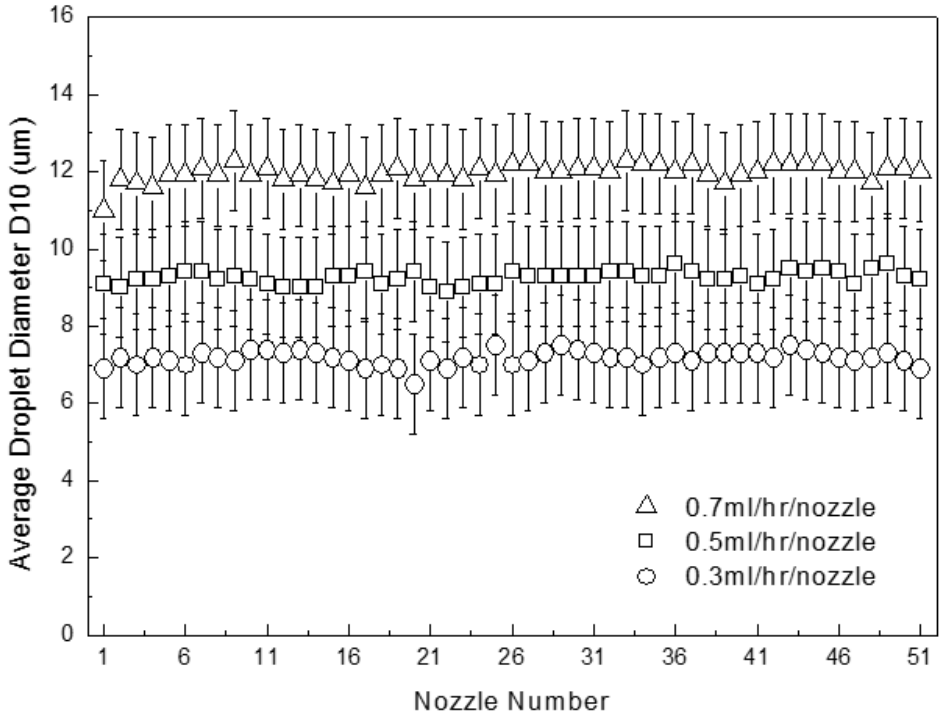

Figure 21: Average droplet diameter across the 51 nozzle LINES array at varied flow rates

CHAPTER 4: MULTIPLEXED ELECTROSPRAY DEPOSITION OF TITANIA NANOPARTICLE THIN FILMS

To characterize the coating performance of LINES, a 25 nozzle device (P=1mm, ID=100μm, L=1.8mm) was integrated as the showerhead for a coating system with a linear stage and heated substrate. The system was designed specifically to provide a benchmark representation of the deposition patterns resulting from a linear electrospray arrays. Titania nanoparticles were chosen as the standard coating material due to their widespread applications as a photocatalyst, pigment, and semiconductor. Silicon wafers were used as the substrate because of their low surface roughness, conductivity, and grayscale contrast with the white titania. The driving field, substrate speed, and direction were varied and the resulting films were characterized using SEM, optical profilometry, and macro photography to measure the coating thickness and visualize the nanoparticle film morphology. The micrographs were then compared against thickness and width estimates from a simple mass balance model, line-of charge model, and GPU simulation.

4.1 Coating System

A system was designed to benchmark the coating performance of LINES. An image of the system is provided in Figure 22. LINES was mounted and enclosed in a custom designed 80/20 frame standing roughly 33”x20”x36” (width, depth, height). The system utilized two Acopian high voltage power supplies (P020HP1.5M) to drive up to 20kV at 1.5mA to the distributor and extractor. A New Era Pump Systems NE-300 Syringe pump was used to feed the suspension to

the reservoir of the distributor. A 7”x7” Cole-Parmer StableTemp™ Ceramic Hot Plate was mounted to a Servo Systems 12” linear stage (MLPS-12-10). LINES was mounted above the motion controlled heat plate and could be adjusted to change the extractor to collector (substrate) distance. A 12x4 grid of 48 white LEDs with a Teflon diffuser to even distribute light was mounted behind LINES to illuminate each nozzle-tip. A Canon EOS600D camera with EF100mm f/2.8L Macro IS USM lens was mounted on a 4”x4” XY stage to visualize each nozzle tip. A TB6560 stepper motor driver controlled by EMC2 was used to drive the XY Camera stage and the substrate stage. The image from the camera was displayed on a 21” Dell LCD to visualize the tip of each nozzle while varying the electrode voltages and liquid flow rate. A custom substrate clamping arm was designed to mechanically fix and electrically ground the substrate during coating.

Figure 22: LINES thin film deposition system

4.2 Nanoparticle suspension

To get an accurate depiction of the deposition pattern resulting from LINES, titania nanoparticles were chosen as the tracer material to represent the trajectories of the droplets emitted. Titania nanoparticles with 20nm average diameter (Degussa P25) were suspended in ethanol at

0.45% wt/wt. A stable nanoparticle suspension was made by mixing a higher concentration suspension of 2% wt/wt. The suspension was sonicated for 24 minutes and allowed to rest undisturbed for 36 hours, after which, the large aggregate particles settled at the bottom of the container. The nanoparticles that remained stabilized due to electrostatic surface charge were then skimmed off into a separate container. In large aggregate particles, gravity dominates the electrostatic suspending force provided by surface charge due to the low surface to volume ratio, so the particles settle over time. The stable suspension was verified to be 0.45 wt% by weighing a out a couple milliliters of suspension, evaporating the ethanol, and then weighing the dried titania nanoparticle remnants.

To verify the separation of large aggregates and nanoparticles, the unstable aggregate and stable nanoparticle suspensions were each coated on a silicon wafer using spin coating and visualized using SEM. The SEM images show distinct distribution of large aggregates from the settled suspension and nanoparticles from the stable suspension. Due to the nature of spin coating, it is expected that the solvent evaporation and fluid flow might cause some aggregation during the spin coating process. Nonetheless, the SEM images still reveal an obvious difference between the suspensions, as seen in Figure 23. The unstable suspension consists of large micron sized aggregates while the skimmed suspension contains mostly submicron particles with few micron aggregates. Some circulation within the flow inlet during the skimming process was noticed and might explain why there are some micron sized particles in the skimmed solution.

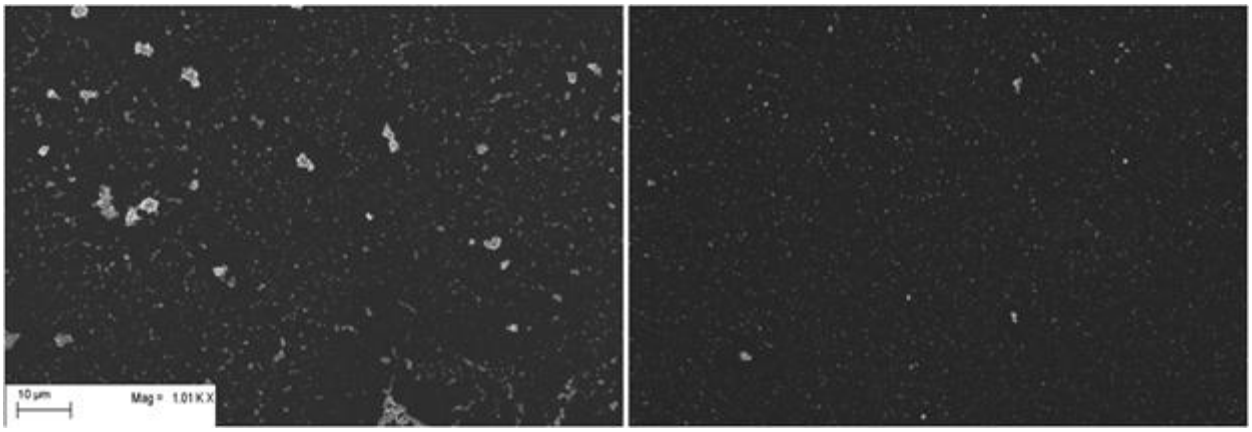

Figure 23: SEM image of aggregate suspension (left) and stable nanoparticle suspension (right)

To gain a more quantitative understanding of the two suspensions, ImageJ was used to obtain a representative distribution of the particle size in each solution from the SEM images. The 1000x magnified images of the spin coated samples were made binary by using the make binary command in ImageJ. Then the analyze particles function was used to measure the area of the discrete particles in each image. The area fraction covered by the particles in the images of the aggregated suspension and stable nanoparticle suspension were 2.9% and 1.9%, respectively. The area distribution of the particles was then divided into particle size bins limited by the resolution provided by the image size and scale. At 1000x, one pixel is approximately 250nm in diameter, and so this is the limit of the smallest particle size measureable. This might also explain this difference in area fraction although the suspension weight fractions were the same, being that the contrast of smaller particles might not be significant enough to invert the pixel upon using the 'make binary' command. Counts for the number of particles in each bin were normalized by the total area covered by the particles to obtain the area percentage of each particle size bin. In the stable suspension it was found that 64% of the particles were 250nm in diameter or smaller. In the

unstable suspension, 69% of the particles were larger than 250nm in diameter. The area percentage results for particles up to 456nm in diameter (0.208μm^2) are presented in Figure 24. This data demonstrates that the skimming method is sufficient in separating the large aggregated particles from the separated nanoparticles to obtain a stable suspension.

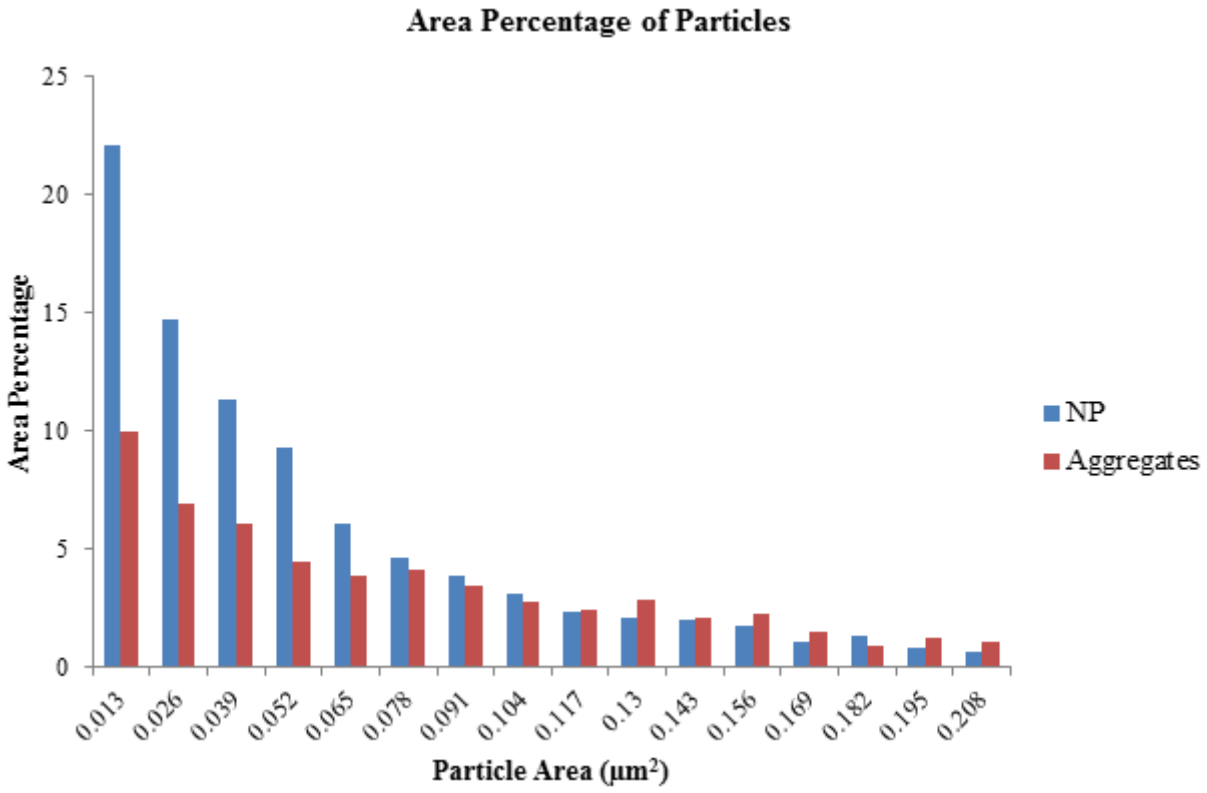

Figure 24: Distribution of particle sizes from the SEM images of the stable and aggregate nanoparticle suspensions

By ensuring that the particles are actually nanoparticles, clogging of the 50μm nozzles is alleviated. Smaller particles are advantageous for precisely controlling the thickness of a coating, since the particles inherently determine the film morphology. For example, making a 10μm thick coating is impossible using 50μm particles. Since the particles act as the building blocks of the

coating, it is intuitive for the particle diameter be at least an order of magnitude smaller than the coating thickness so that multiple particles must add up to build the coating.

4.3 Nanoparticle Deposition Procedure

The stable suspension was sonicated for 24 minutes prior to loading in the syringe for the deposition experiments and was electrosprayed through the 25 nozzle LINES at a total flow rate of 12.5 ml/hr (0.5 ml/hr per nozzle) onto a heated silicon wafer. Prior to coating, the silicon wafers were thoroughly cleaned using a sequential rinse in acetone, ethanol, and deionized water. The LINES device was verified to be spraying in the cone-jet mode prior to initiating the substrate motion using the camera system. The substrate moved at a constant speed of 2.4 cm/min over the deposition area. This scanning type motion was repeated back and forth 5 times to produce a film around 10μm thick. The speed and liquid flow rate were kept constant for all experiments, while the substrate temperature, driving field, and substrate motion angle were varied. A summary of the coating conditions for the four experiments are presented in Table 6.

Table 6: Summary of coating conditions

Sample	Substrate Temperature (°C)	Driving Field (kV/cm)	Angle (deg)
A	70	3.33	90
B	70	5.67	90
C	130	5.67	90
D	70	5.67	45

4.4 Coating Results

The resulting film under the four operating conditions were analyzed with macro photography, SEM, and optical profilometry to determine the profile width, edge width, thickness, surface roughness, and morphology. A summary of the results are presented in Table 7. The following sections describe the methodology for obtaining the values presented.

Table 7: Summary of coating results

Sample	Macro Photograph		SEM Results			Optical Profilometer	
	Pattern Width (mm)	Edge width left/right (mm)	Coating thickness (µm)	Rq (µm)	Rt (µm)	Rq (µm)	Rt (µm)
A	40.8	8.08/8.29	9.03	0.258 (2.86%)	1.32	0.255	2.37
B	35.0	3.74/5.11	9.40	0.364 (3.87%)	2.17	0.190	1.47
C	36.2	3.63/5.6	10.7	0.300 (2.82%)	1.76	0.160	1.25
D	26.2	3.17/3.8	13.3	0.201 (1.44%)	1.76	0.450	2.97

4.4.1 Width and Edge

The four samples were imaged using a Canon Rebel T2i with a Sigma f/2.8 50mm Macro Lens. The images were taken using identical lighting conditions from an overhead white LED lamp using a 10ms exposure, ISO-400, and f/8. The resulting images for the four samples are presented in Figure 25. The images allowed analysis of the coating width, edge width, and thickness variation patterns over the width.

The pictures were post-processed in ImageJ by first converting the images to 8-bit grayscale and then using the despeckle function to remove some of the light noise. The scale was set using an image of a ruler. A line was drawn perpendicular to the direction of motion and the grayscale intensity of each pixel was obtained as a function of distance. This provides a

representation of the the crossection coating pattern. The average grayscale value in the center 10mm of the profile (where the thickness was flat and maximum) was used to normalize the grayscale profile to a unit scale which could then be multiplied by the SEM average thickness and plotted in units of microns, as seen in Figure 25 – Top. The micron thickness scale provides a more meaningful image rather than a relative pixel grayscale value and shows that the electric field has the most significant effect on the edge width and slope.

Both Table 7 and Figure 25 demonstrate that increasing driving field decreases spray width and increasing temperature increases spray width. This is intuitive and agrees with Eqs. 4 and 7, that under driving weaker driving fields the spray expands more. The increase in temperature increases the thermal vibration energy of atoms at the substrate which lends itself to spreading out droplets and nanoparticles further. Sample A was at the lowest temperature, 70°C, and driving field, 3.33kV/cm, therefore, the droplets evaporated slowest and arrived with the lowest velocity and expanded the most to produce the widest coating of all the samples. Sample B was the same as A, but at a 1.7 times stronger driving field. Thus, the droplets here had a higher incoming velocity and the spray footprint was narrower since the residence time was decreased and the droplets had less time to expand from Coulombic repulsion. Sample C has the same driving field as B, but the higher temperature produced a wider footprint and edge. Sample D with the same conditions as C but with a 45 degree angle exhibited the most narrow footprint and the sharpest edge due to the overlapping spray plumes.

The edge of the deposition pattern varied considerably under varied operating conditions. Higher driving fields tend to lead to steeper edges, while the edge is more dispersed under low

driving fields. So for coating applications requiring a sharp, well defined coating edge, high driving fields are desirable. The fact that the left edge width was smaller that the right edge width for all cases might be attributed to a variation in the extractor to collector distance, i.e. the right extractor edge was likely at a larger distance from the collector than the left edge. In all of the cases a two-slope trend is seen, where the edge slope increases sharply from the local number density ditribution within the edge spray plume, then the slope decreases slowly as the spray plumes overlap towards the center of the spray.

To quantify the edge width, the edge limit was defined by the thickness reaching 90% of the average thickness of the center 10mm. The grayscale the film edges are plotted in Figure 25 - Bottom and the width values are provided in Table 7. Both the left and right edges are presented as two separate lines, with Sample C showing the greatest difference in the left and right edges, wheras Samples A, B, and C are more symmetric. Samples B, C, and D were all coated at 5.67 kv/cm and all exhibit the same initial edge slope, while sample A, which was coated at 3.33 kv/cm, has a distincively lower initial edge slope. Intuitively, the highest driving field and overlapping spray plumes of Sample D produced the thinnest edge whereas the lowest driving field, Sample A, produced the widest edge.

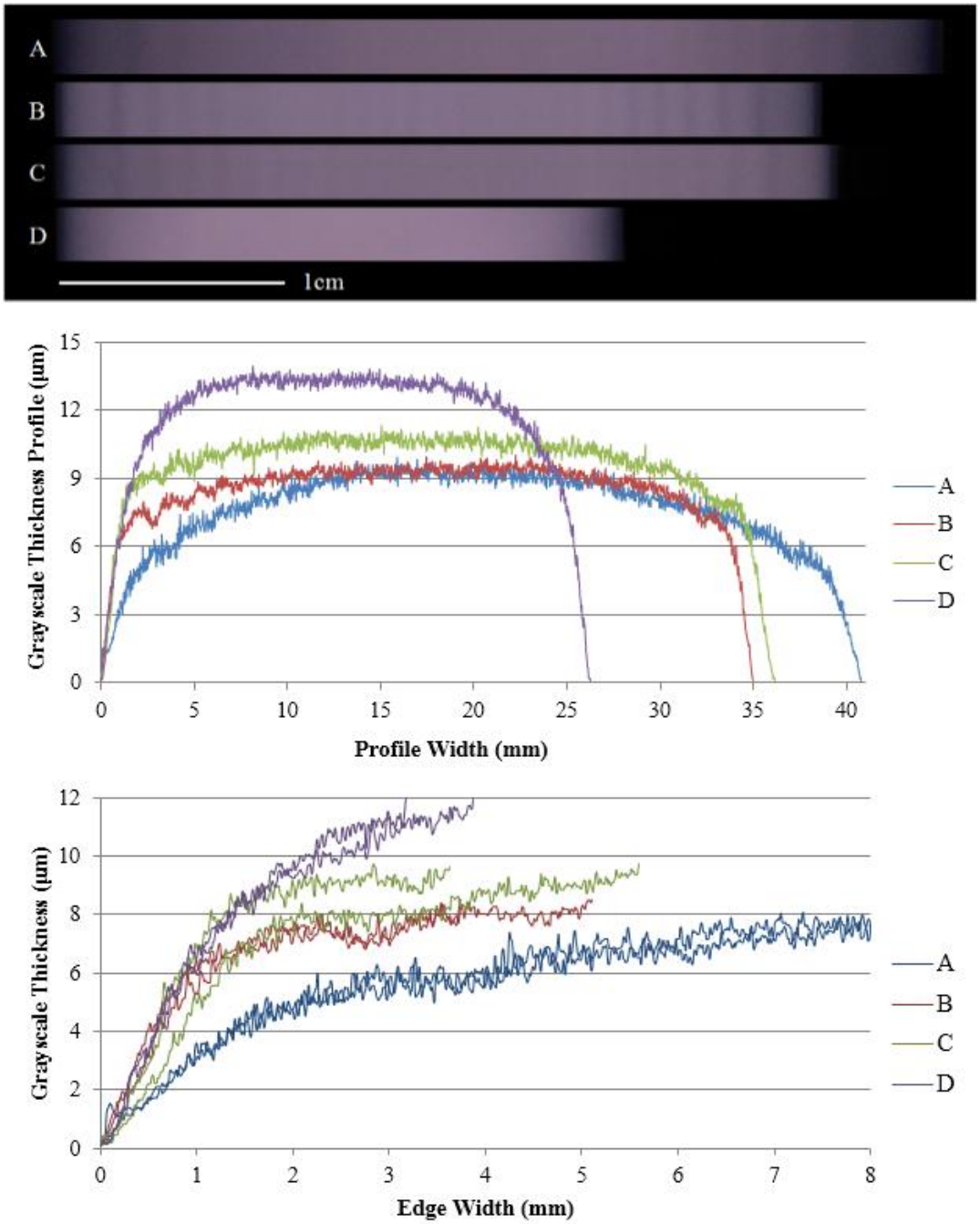

Figure 25: Macro photographs of coating samples showing the width, edge, and wave pattern (top), grayscale thickness profile from macro images (middle), edge profile from macro images (bottom).

4.4.2 Thickness and Density

To estimate the average thickness of the coating, t, a simple model was employed based on conservation of mass; i.e. the mass of solids in suspension is equal to the mass of the film. This is simplified in Equation 10 as:

$$t = \frac{Qc}{\rho w v \sin\theta} \tag{10}$$

where Q is the liquid flow rate (ml/min), c is the weight concentration of the liquid (mg/ml), ρ is the film density (mg/ml), v is the substrate velocity (cm/min), and θ is the angle of the substrate velocity vector with respect to the LINES array (degrees). The density is a crucial characteristic which defines the film, and it is important to have an accurate value. This equation presupposes the film density is known. The complexities of the film building process with evaporation, aggregation, etc. makes it very difficult to estimate the film's inherent porous aggregate structure. Using the tapped density of P25 which is 130mg/ml (Aeroxide P25), provides a reasonable basis point. To get an acutal density value, the measured film thicknesses presented in Table 7 can be used to back calculate the density. Using sample A, the film density was calculated to be 97.8 mg/ml, or about 75% of the tapped density of P25 powder and 2% of the bulk density of TiO2. Thus, the films obtained are highly porous and of low density by nature.

Using the 4000x cross section SEM images, the local coating thickness and surface roughness was was meaured in ImageJ and analyzed with the Distance Between Lines plugin. This plugin allows calculation of the average distance and standard deviation between the substrate to coating surface of a cross sectional image. A linear line is first drawn on the substrate surface and

a segmented line is drawn on the uneven coating surface. The plugin then measures the distance between these two lines at 0.5μm increments over the span width and calculates the average distance and standard deviation, which is presented in Table 7 for the four experiments as the average thickness and surface roughness.

The low temperature and driving field conditions of Sample A lead to the thinnest film. Samples B and C were at a more intense electric field, but C was at a higher temperature. It is intuitive for a more narrow spray width to produce a thicker coating. Sample B was thicker than A and Sample C was thicker than Sample B. Sample D was the same as B, but at a 45 degree substrate angle. This lead to a thicker coating from the spray plumes overlapping the same area. The thickness data implies that temperature increase leads to an increase in the film thickness and porosity and decrease in the density.

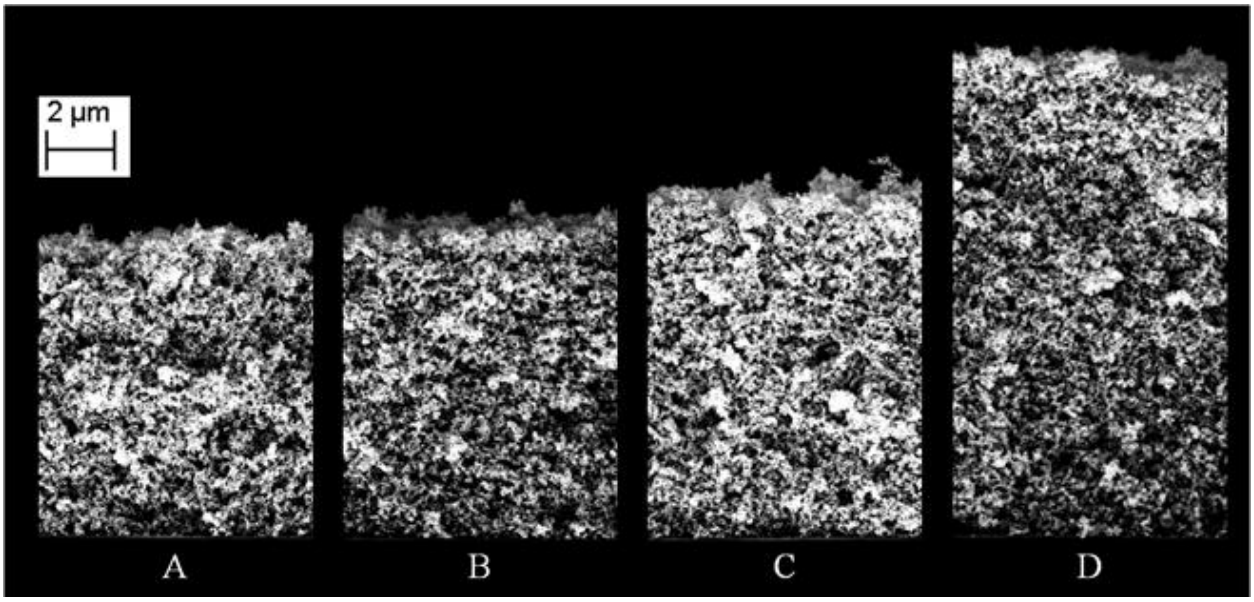

Figure 26: SEM image of coating thickness cross-section at 4,000x magnification

4.4.3 Surface Roughness and Film Morphology

Surface roughness is defined by a dataset of thickness measurement points. The standard deviation between each measured point to the average is given by R_q. The local R_q surface roughness was calculated using the 4,000x magnification SEM images by the same way as the thickness was measured, using the Distance Between Lines Plugin. The peak to peak distance, R_t, was height between the lowest and highest points on the coating surface was measured on the 4,000x SEM images. The results presented in Table 7 for the four experiments show that sample D at the 45° angle produced the lowest R_t and R_q values, while sample B at the highest driving

field and lowest temperature produces the greatest R_t and R_q values. The R_t and R_q values were also obtained using an Veeco Optical Profilometer, as seen in Table 7 showing good agreement.

At the macro, mm length scale, streaks in the film can be seen with the naked eye and the film appears to be non-uniform. This is clearly seen in the macro images featured in Figure 25 - Top. An estimate of the 'long wavelength' pattern which is a result of the repulsion of neighboring spray plumes by dividing the pattern width by number of electrospray nozzles in the array gives. In this case of B, this wavelength is approximately 1.4mm, which agrees very well with the wavelength measured from the Figure 25. The peak to peak R_t value for these waves ia approximately 1μm. These waves are more distinct at the edge of the film since the space charge is less intense at the edge of the array. A wave pattern is distinct for samples A, B and C, especially at the edge of the sample, due to the weaker electric field.

The film morphology is presented in Figure 27 showing the microstructure at 1,000x magnification and the nanostructure at 20,000x magnification. At the micron and nanometer scales, there was not very much variation in the film morphology under varied driving fields, temperatures and angles. Under all conditions, the morphology consists of a network of agglomerated nanoparticles. The microstructure shows a distinct 'white noise' pattern with the agglomerates and pores on average around 0.4μm in length. There are some sporadic large spherical agglomerates around 1μm in diameter which are thought to have come from agglomerates formed within the LINES device due to fouling. In the nanostructure SEM images,

the individual 20nm titania nanoparticles that make up the larger ~0.4μm agglomerates can be distinguished.

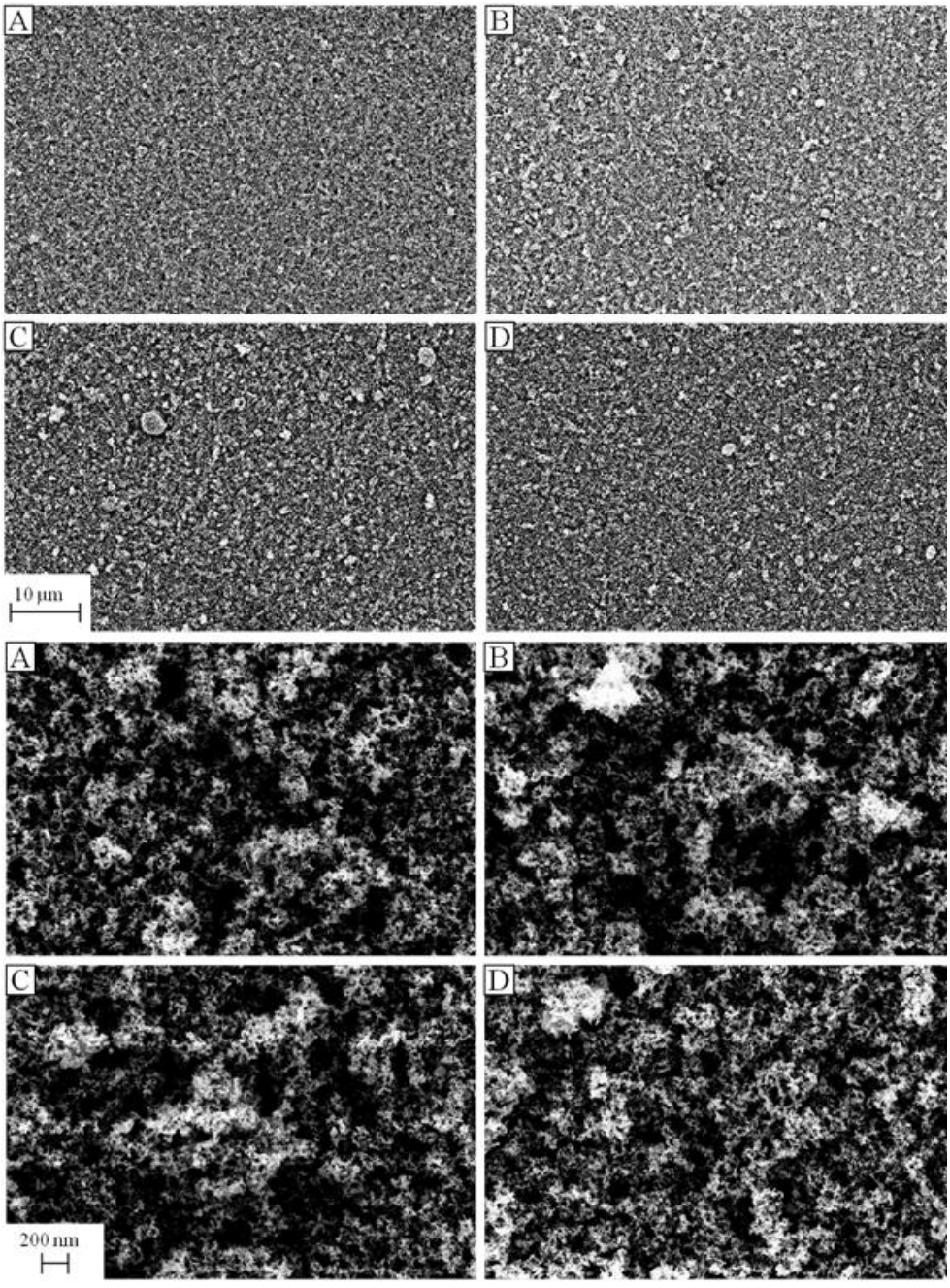

Figure 27: SEM images of coating morphology, microstructure at 1,000x magnification (top), Nanostructure at 20,000x magnification (bottom)

Both the high driving field samples B and C show aggregate pillar structures emanating from the surface, seen in Figure 28. It is possible that these structures are a result of the high driving field leading to more preferential droplet trajectories so that pillar structures are built upwards from droplets landing in a common place. The film morphology appears to be more densely packed in sample D, which might be a result of the higher frequency of incoming droplets. The higher the driving field is, the higher the velocity of the incoming droplet. Lower velocity leads to a more gentle impact, and less chance of rebounding droplets. The higher the substrate temperature is, the higher the evaporation rate of the incoming droplet. Lower temperature means slower evaporation which provides more time for the droplets to spread over the surface after landing, as opposed to immediately evaporating. Moreover, rapid evaporation leads to convection at the surface due to the vapor generation. This convection tends to generate a more porous coating as the vapors are escaping as the film is solidifying.

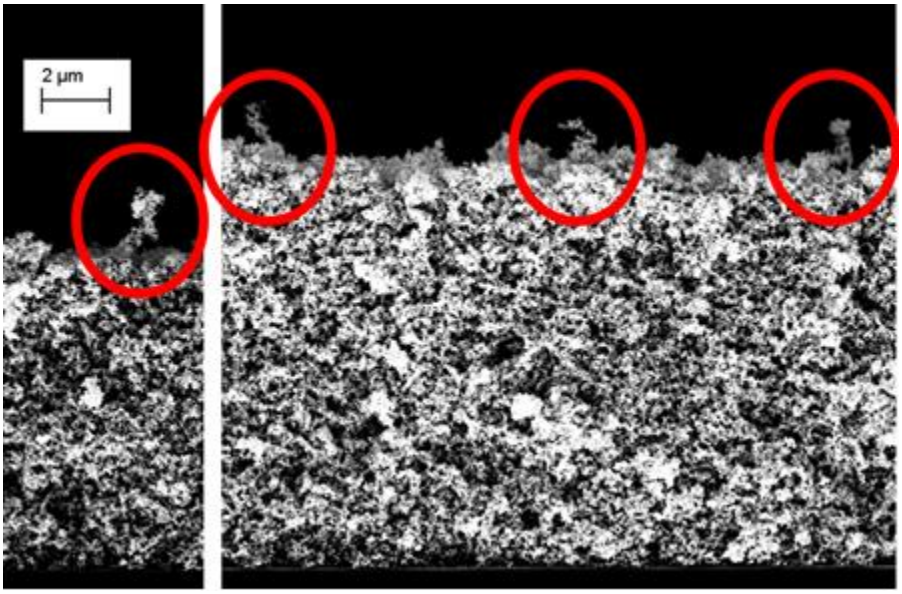

Figure 28: Aggregate pillar structures

4.5 GPU Simulation

The same GPU model that was discussed in 3.2 was run again to simulate the interactions of droplets from the 25 nozzle LINES array. This time the resulting droplets were analyzed for comparison against the spray footprint obtained during the coating experiments.

The model was run under the same conditions as experiment s B and C until approximately 10^5 droplets were collected at the substrate. Note that thermal effects, and thus temperature is not incorporated into the model. Considering each electrospray source is emits 10^6 droplets per second, and there are 25 nozzles, 10^5 droplets represents about a 20ms dose of droplet flux. This is just a

brief snapshot of a much more simplified deposition process and does not allow for a direct comparison with the coating experiments. However, it does provide useful insight into the deposition from MES sources.

The deposition from the simulation is simplified by taking a planar cross-section parallel with the extractor 3cm away from jet-break-up to simulate the substrate. This plane was broken into a 500x500 grid (each cell 80 μmx80μm) and the droplet flux thru each cell was recorded as a 2D number density plot. The number density for the 10^5 dose can be seen in Figure 29, which agrees in terms of footprint size and also captures the wave pattern at the edge from the fanning and segregation of individual spray plumes. The plot appears grainy compared to the macro image surfaces due to the relatively large cell size.

A cross section of the *x*-*z* plane surface is provided in Figure 30 - Top and compared against Sample B, since the conditions of the GPU simulation best match sample B. The edge profiles for the GPU simulation and Sample B are presented in Figure 30 - Bottom, which somewhat agree in terms of slope. The GPU simulation was unable to capture the dual slope edge that is distinct in Figure 25 - Bottom.

The GPU data was normalized by the average number density of the center 10mm span. The R_q surface roughness for the center 10mm span of the profile are 11.1% and 3.87% for the GPU simulation and sample B, respectively. One reason for the large discrepancy in the roughness values between experiment and GPU simulation is the averaging nature of the nanoparticle film growth process.

The result here shows that electrospray tends to create interesting fractal like structures when nanoparticle suspensions are deposited on flat surfaces. This leads to porous structures which cannot be simulated in the GPU software. These structures bridge and create voids which incoming droplets can't fill. This overall leads to a more uniform coating surface as the particles build up. The simulation is an idealized case with fewer forces at work than in the experiment, with other effects such as evaporative flow and nanoparticle Van der Waals forces. Also discrepancies in the measured current which had to be input to the simulation may have cause inconsistencies between the simulation and experiment.

It is interesting to see how the surface roughness becomes more even when the GPU data is simulated with relative substrate motion. This is due to an averaging effect of the edge and center. A true representation could be attained by running the simulation for much longer, precisely, the coating width divided by the velocity, which is about 25 seconds. This is 1000 times longer than the simulation was actually run to produce the data in Figure 29, which took 1 day in reality.

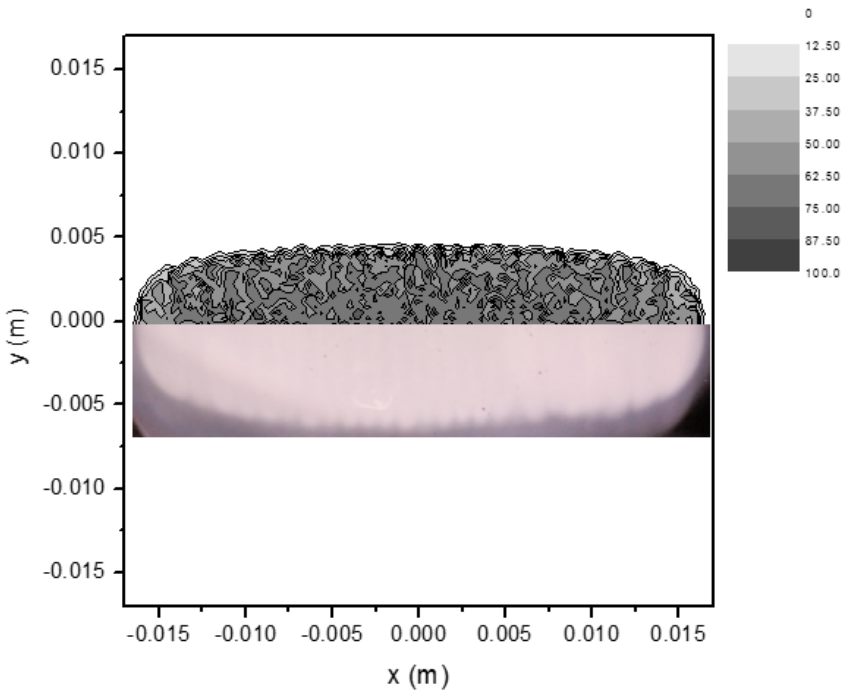

Figure 29: Deposition number density plot from a static 25 nozzle GPU simulation (top) overlaid with a static deposition footprint from experiment (bottom)

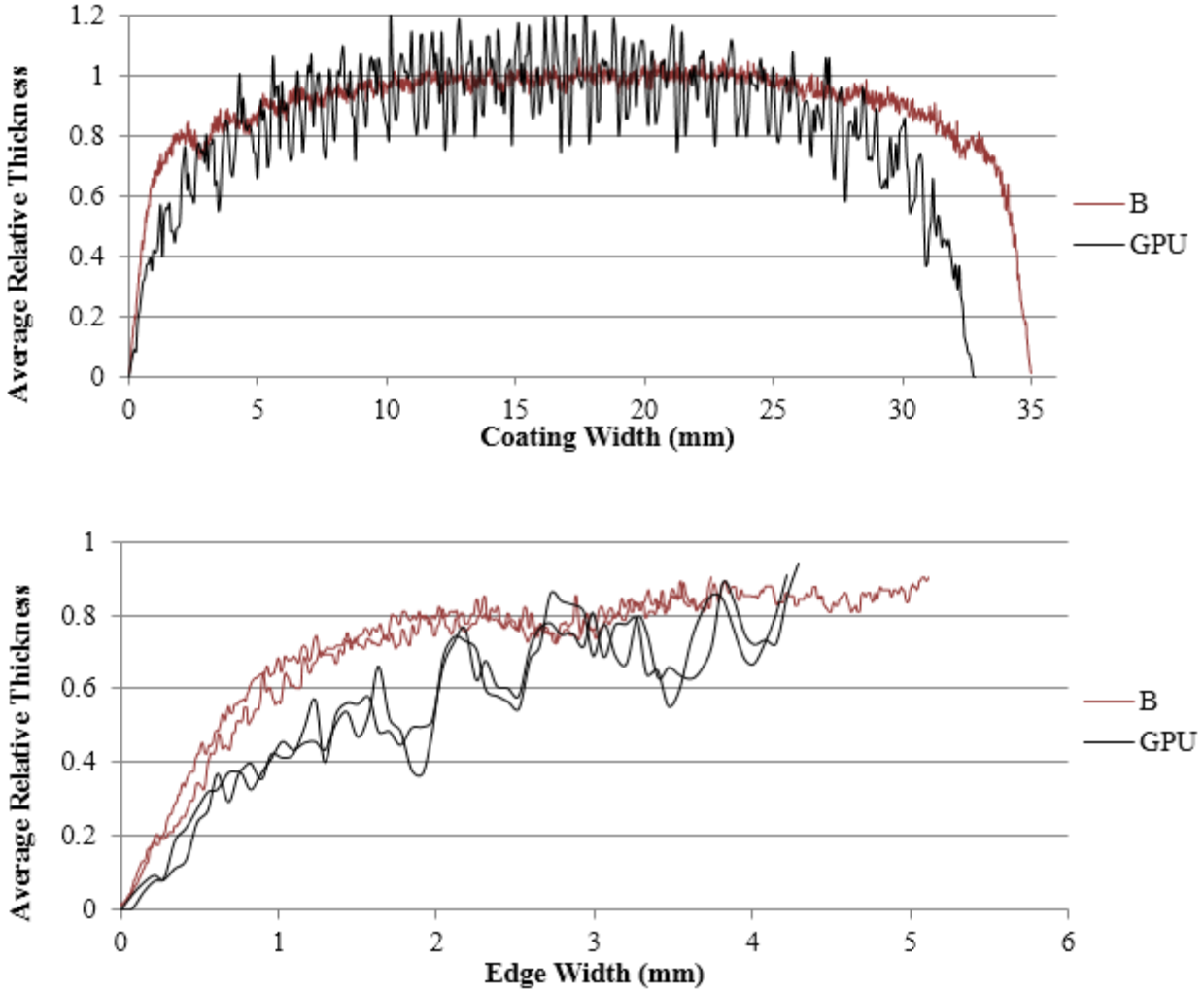

Figure 30: Comparison of GPU and sample, average relative thickness over coating width (top), average relative thickness edge profile (bottom)

CHAPTER 5: CONCLUSION AND RECOMMENDATIONS

This chapter concludes the thesis, providing a review of the results and recommendations for moving forward with using MES technology for coating applications.

5.1 Conclusions

It is concluded that the MES technique is suitable for applying porous nanoparticle coating with micron scale thickness. Such a film can find application in dye sensitized solar cells where the TiO_2 layer must be highly porous to facilitate the dye and a high surface area to pore volume for absorption of incoming light.

The spray profile model and GPU simulation are useful for determining the required operating conditions for MES devices and the resulting spray foot print area. It is difficult to use the simulation data in terms of droplet flux density and extend this to provide information about the surface patterns. The resolution of the simulation becomes limiting and the resulting coating morphology becomes less dependent upon the flux distribution and more dependent upon the molecular or particle level domain of interaction at the substrate. The foot print data does give an area which can be implemented into a simple mass balance thickness calculation. A factor of the relative density of the resulting film compared to the bulk material can be extracted experimentally and used to accurately estimate the thickness there forward.

5.2 Recommendations

Due to limited time and the complexity of setting up and operating the LINES device, experiments were limited. Future work will utilize the equipment to get a wider sample population and provide results with higher confidence.

A flow through reactor might be favorable for CVD reactions which require high temperatures. In high temperature scenarios, the showerhead might be overheated, leading to issues with solvent evaporation at the cone surface and possibly inhibiting continuous operation of cone-jet electrospray. By having a flow through reactor, the MES atomizer could be kept upstream in a cool region to deliver aerosol precursors to a hot reaction zone. Another possible solution is to design a cooling extractor which serves not only as an electrostatic shield, but also as a thermal shield to protect the cone-jet forming region from the spray forming region.

A key point to extract from the coating experiments are that with higher levels of mixing and spreading, the more uniform the spray footprint becomes. In cases of high electric fields, the spray plumes become segregated and a distinct streak pattern is seen in the film. However, under weaker fields and when the spray plumes overlap, the droplet flux becomes more uniform and the streak pattern become less distinct. The more uniform the flux is, the more uniform the film is, and the more accurate the mass balance calculation (Eq. 10) for thickness becomes. When the flux is uniform enough, this simple calculation might find great usefulness in a coating system capable of depositing a film of a user entered thickness, where a precursor dose might be dispensed and delivered to a substrate over a known area, to result in a film with predetermined density. In that way a user could specify a coating thickness and automatically obtain that through a control system

with a calibrated film density value. The control could be further enhanced by closing the loop with a thickness monitor to measure the growth rate, such as a profilometer.

Additionally, for mass manufacturing of MES nozzles, an injection molding or other rapid parallel fabrication approach such as soft lithography. The serial nature of machining processes would become prohibitively time consuming for manufacturing large volumes of MES arrays containing thousands of nozzles.

LIST OF REFERENCES

Almekinders, J.C., and C. Jones. 1999. "Multiple jet electrohydrodynamic spraying and applications." *Journal of Aerosol Science* 30: 696-671.

Almería, B., W. Deng, T.M. Fahmy, and A. Gomez. 2010. "Controlling the morphology of electrospray generated PLGA microparticles for drug delivery." *Journal of Colloid and Interface Science* 343: 125-133.

Arnanthigo, Y., C. U. Yurteri, J.M. Marijnissen, and A. Schmidt-Ott. 2009. "Multiple Electrospray Unit with Circular Symmetry." *European Aerosol Conference.* Karlsruhe.

Arnanthigo, Y., C.U. Yurteri, G. Biskos, J.C.M. Marijnissen, and A. Schmidt-Ott. 2011. "Out-scaling electrohydrodynamic atomization systems for the production of well-defined droplets." *Powder Technology* 214: 382-387.

Ataman, Caglar, Simon Dandavino, and Herbert Shea. 2012. "Wafer-level integrated electrospray emitters for a pumpless microthruster system operating in high efficiency ion-mode." *2012 IEEE 25th International Conference on Micro Electro Mechanical Systems.* Paris. 1293-1296.

Balachandran, W., P. Miao, and P. Xiao. 2001. "Electrospray of fine droplets of ceramic suspensions for thin-film preparation." *Journal of Electrostatics* 249-263.

Biltoft, J. P., M. A. Benapfl, and T. Swain. 2002. *Vacuum Technology: an introductory laboratory course.* Livermore, California: Las Positas College.

Blades, A.T., M.G. Ikonomou, and P. Kebarle. 1991. "Mechanism of Electrospray Mass Spectrometry. Electrospray as an Electrolysis Cell." *Analytical Chemistry* 63: 2109-2114.

Bocanegra, R., D. Galán, M. Márquez, I.G. Loscertales, and A. Barrero. 2006. "Multiple electrosprays emitted from an array of holes." *Journal of Aerosol Science* 36: 1387-1399.

Byrappa, K., and T. Adschiri. 2007. "Hydrothermal technology for nanotechnology." *Progress in Crystal Growth and Characterization of Materials* 117-166.

Chen, C.H., E.M. Kelder, M.J.G. Jak, and J. Schoonman. 1996. "Electrostatic spray deposition of thin layers of cathode materials for lithium battery." *Solid State Ionics* 86-88: 1301-1306.

Chen, D.R., and D.Y.H. Pui. 1997. "Experimental investigation of scaling laws for electrospraying: Dielectric constant effect." *Aerosol Science and Technology* 27 (3): 367-380.

Choi, K.H., K. Rahman, A. Khan, and D.S. Kim. 2011. "Cross-talk effect in electrostatic based capillary array nozzles." *Journal of Mechanical Science and Technology* 25 (12): 3035-3062.

Cloupeau, M., and B. Prunet-Foch. 1989. "Electrostatic spraying of liquids in cone-jet mode." *Journal of Electrostatics* 22 (2): 135-159.

De Juan, L., and J. Fernández de la Mora. 1997. "Charge and size distribution of electrospray drops." *Journal of Colloid and Interface Science* 186: 280-293.

Deng, W., and A. Gomez. 2011. "Electrospray cooling for microelectronics." *International Journal of Heat and Mass Transfer* 54: 2270-2275.

Deng, W., and A. Gomez. 2007. "Influence of Space Charge on the Scale-up of Multiplexed Electrosprays." *Journal of Aerosol Science* 38: 1062-1078.

Deng, W., C.M. Waits, B. Morgan, and A. Gomez. 2009. "Compact multiplexing of monodisperse electrosprays." *Journal of Aerosol Science* 40: 907-918.

Deng, W., J.F. Klemic, X. Li, M. Reed, and A. Gomez. 2006. "Increase of electrospray throughput using multiplexed microfabricated sources for the scalable generation of monodisperse droplets." *Journal of Aerosol Science* 37: 696-714.

Deng, W., J.F. Klemic, X. Li, M. Reed, and A. Gomez. 2007. "Liquid Fuel Combustor Miniaturization via Microfabrication." *Proceedings of the Combustion Institute* 31: 2239-2246.

Dobkin, D.M., and M.K. Zuraw. 2003. *Principles of Chemical Vapor Deposition.* Springer.

Duby, M.H., W. Deng, K. Kim, T. Gomez, and A. Gomez. 2006. "Stabilization of monodisperse electrosprays in the multi-jet mode via electric field enhancement." *Journal of Aerosol Science* 37: 306-322.

Fenn, J.B., M. Mann, C.K. Meng, S.F. Wong, and C.M. Whitehouse. 1989. "Electrospray ionization for mass spectrometry of large biomolecules." *Science* 246: 64-71.

Fernández de la Mora, J. 1992. "The effect of charge emission from electrified liquid cones." *Journal of Fluid Mechanics* 243: 561-574.

Fernández de la Mora, J. 1992. "The effect of charge emission from electrified liquid cones." *Journal of Fluid Mechanics* 243: 561-574.

Foret, Frantisek, and Petr Kusy. 2006. "Microfluidics for multiplexed MS analysis." *Electrophoresis* 4877-4887.

Ganan-Calvo, A.M., J.C. Lasheras, J. Davila, and A. Barrero. 1994. "Electrostatic spray emitted from an electrified conical meniscus." *Journal of Aerosol Science* 25: 1121-1142.

Gassend, B., L.F. Velásquez-García, A.I. Akinwande, and M. Martínez-Sánchez. 2009. "A Microfabricated Planar Electrospray Array Ionic Liquid Ion Source With Integrated Extractor." *Journal of Microelectromechanical Systems* 679-694.

Gassend, Blaise Laurent Patrick. 2007. *A Fully Microfabricated Two-Dimensional Electrospray Array with Applications to Space Propulsion.* Doctoral Dissertation. Cambridge: Massachusetts Institute of Technology.

Gibson, G.T.T., S.M. Mugo, and R.D. Oleschuk. 2009. "Nanoelectrospray Emitters: Trends and Perspective." *Mass Spectrometry Reviews* 918-936.

Gomez, A., D. Bingham, L. De Juan, and K. Tang. 1998. "Production of protein nanoparticles by electrospray drying." *Journal of Aerosol Science* 29 (5-6): 561-574.

Goodnick, S., A. Korkin, P. Krstic, P. Mascher, J. Preston, and A. Zaslavsky. 2010. "Semiconductor nanotechnology: novel materials and devices for electronics, photonics, and renewable energy applications." *Nanotechnology.*

Hubacz, A.N., and J.C.M. Marijnissen. 2003. "The scale-up of electrohydrodynamic atomization." *Journal of Aerosol Science* 43(Suppl. 1): S1269-S1270.

Jaworek, A. 2007. "Electrospray droplet sources for thin film deposition." *Journal of Materials Science* 42: 266-297.

Jaworek, A., and A.T. Sobczyk. 2008. "Electrospraying route to nanotechnology: An overview." *Journal of Electrostatics* 66: 197–219.

Jaworek, A., M. Lackowski, A. Krupa, and T. and Czech. 2006. "Electrostatic interaction of free EHD jets." *Experiments in Fluids* 40: 568-576.

Kelly, R.T., J.S. Page, I. Marginean, K. Tang, and Smith R.D. 2008. "Nanoelectrospray Emitter Arrays Providing Interemitter Electric Field Uniformity." *Journal of Analytical Chemistry* 5660-5665.

Kelly, R.T., J.S. Page, R. Zhao, W.J. Qian, H.M. Mottaz, K. Tang, and R.D. Smith. 2008. "Capillary-Based Multi Nanoelectrospray emitters: Improvements in Ion Transmission Efficiency and Implementation with Capillary Reversed-Phase LC-ESI-MS." *Analytical Chemistry* 80: 143-149.

Kim, J.S., and D.R. Knapp. 2001. "Miniaturized multichannel electrospray ionization emitters on poly(dimethylsiloxane) microfluidic devices." *Electrophoresis* 22: 3993-3999.

Kim, W., M. Guo, P. Yang, and D. Wang. 2007. "Microfabricated Monolithic Multinozzle Emitters for Nanoelectrospray Mass Spectrometry." *Analytical Chemistry* 79: 3703-3707.

Lenguito, G., J. Fernandez de la Mora, and A. Gomez. 2010. "Multiplexed Electrospray for Space Propulsion Applications." *46th AIAA Joint Propulsion Conference.* 6521.

Lhernould, M.S., and P. Lambert. 2011. "Compact polymer multi-nozzles electrospray device with integrated microfluidic feeding system." *Journal of Electrostatics* 69 (4): 313-319.

Li, K.Y., H. Tu, and A.K. Ray. 2005. "Charge limits on droplets during evaporation." *Lagmuir* 21: 3786-3794.

Lojewski, B., W. Yang, H. Duan, C. Xu, and W. Deng. 2012. "Design, Fabrication, and Characterization of Linear Multiplexed Electrospray Atomizers Micro-Machined from Metals and Polymers." *Aerosol Science and Technology* 146-152.

Mao, P., H.T. Wang, P. Yang, and D. Wang. 2011. "Multinozzle Emitter Arrays for Nanoelectrospray Mass Spectrometry." *Analytical Chemistry* 83: 6082-6089.

Mattox, D. 2010. *Handbook of Physical Vapor Deposition (PVD) Processing.* William Andrew.

Oh, H., K. Kim, and S. Kim. 2008. "Characterization of deposition patterns produced by twin nozzle electrospray." *Journal of Aerosol Science* 39 (9): 801-813.

Oh., H., K. Kim, and S. Kim. 2008. "Characterization of deposition patterns produced by twin-nozzle electrospray." *Journal of Aerosol Science 39* 9: 801-813.

Regele, J.D., M.J. Papac, M.J.A. Rickard, and D. Dunn-Rankin. 2002. "Effects of capillary spacing on EHD spraying from an array of cone jets." *Journal of Aerosol Science* 33: 1471-1479.

Rosell-Llompart, J., and J. Fernandez de la Mora. 1994. "Generation of monodisperse droplets 0.3 to 4um in diameter from electrified cone-jets of highly conducting and viscous liquids." *Journal of Aerosol Science* 25: 1093-1119.

Rulison, A.J., and R.C. Flagan. 1993. "Scale-up of electrospray atomization using linear arrays of Taylor Cones." *Review of Scientific Instruments* 64: 683-686.

Saf, R., M. Goriup, T. Steindl, T. Hamedinger, D. Sandholzer, and G. Hayn. 2004. "Thin organic films by atmospheric-pressure ion deposition." *Nature Materials* 323-329.

Sakiadis, B.C. 1961. "Boundary-Layer Behavior on Continuous Solid Surfaces: III. The Boundary Layer on a Continuous Cylindrical Surface." *American Institute of Chemical Engineers Journal* 7: 467-472.

Serrano, E., G. Rus, and J. Garcia-Martinez. 2009. "Nanotechnology for sustainable energy." *Renewable and Sustainable Energy Reviews* 2373–2384.

Shokeen, M. 2012. "Promise of Nanotechnology in Biomedical Applications." *Journal of Medical Diagnostic Methods* 1-2.

Smith, D. 1995. *Thin Film Deposition Principles.* McGraw-Hill.

Snarski, S.R., and P.E. Dunn. 1991. "Experiments characterizing the interaction between sprays of electrically charged liquid droplets." *Experiments in Fluids* 11: 268-278.

Som, S.K., and S.K. Dash. 1993. "Thermodynamics of spray evaporation." *Journal of Physics D: Applied Physics* 574-584.

Sundaram, K. 2006. *Thin Film Technology*. Orlando: University of Central Florida.

Tai, Y.C., J. Xie, Q. He, J. Liu, and T. Lee. 2002. "Integrated Micro/Nano Fluidics for Massspectrometry Protein Analysis." *International Journal of Nonlinear Sciences and Numerical Simulation* 3: 739-741.

Tang, K., and A. Gomez. 1994. "On the structure of an electrostatic spray of monodisperse droplets." *Physics of Fluids* 6: 2317-2332.

Tang, K., Y. Lin, D.W. Matson, T. Kim, and R.D. Smith. 2001. "Generation of multiple electrosprays using microfabricated emitter arrays for improved mass spectrometric sensitivity." *Analytical Chemistry* 73 (8): 1658-1663.

Tran, S.B.Q., D. Byun, and S. Lee. 2007. "Experimental and theoretical study of a cone-jet for an electrospray microthruster considering the interference effect in an array of nozzles." *Journal of Aerosol Science* 38: 924-934.

Tran, S.B.Q., D. Byun, V.D. Nguyen, H.T. Yudistira, M.J. Yu, K.H. Lee, and J.U. Kim. 2010. "Polymer-based electrospray device with multiple nozzles to minimize end effect phenomenon." *Journal of Electrostatics* 68: 138-144.

Velásquez-García, L.F., A.I. Akinwande, and M. Martínez-Sánchez. 2006. "A Micro-fabricated Linear Array of Electrospray Emitters for Thruster Applications." *Journal of Microelectromechanical Systems* 15 (5): 1260-1271.

Wang, W.Q., A. Desai, Y.C. Tai, L. Licklider, and T.D. Lee. 1999. "Polymer-Based Electrospray Chips For Mass Spectrometry." *Twelfth IEEE International Conference on Micro Electro Mechanical Systems.* Orlando. 523-528.

Wang, Y.X., J.W. Cooper, C.S. Leec, and D.L. DeVoe. 2004. "Efficient electrospray ionization from polymer microchannels using integrated hydrophobic membranes." *LabChip* 4: 363-367.

Xiong, J., Z. Zhaoying, Y. Xiongying, W. Xiaohao, Y. Feng, and Y. Lib. 2002. "A colloid microthruster system." *Microelectronic Engineering* 61-62: 1031-1037.

Xue, Q., F. Foret, Y.M. Dunayevskiy, P.M. Zavracky, N.E. McGruer, and B.L. Karger. 1997. "Multichannel Microchip Electrospray Mass Spectrometry." *Analytical Chemistry* 69: 426-430.

Yang, W., B. Lojewski, Y. Wei, and W. Deng. 2012. "Interactions and Deposition Patterns of Multiplexed Electrosprays." *Journal of Aerosol Science* 46: 20-33.

Yurteri, C.U., R.P.A. Hartman, and J.C.M. Marijnissen. 2010. "Producing Pharmaceutical Particles via Electrospraying with an Emphasis on Nano and Nano Structured Particles - A Review." *KONA Powder and Particle Journal* 91-115.

Zhou, F.L., R.H. Gong, and I. Porat. 2009. "Mass production of nanofibre assemblies by electrostatic spinning." *Polymer International* 331-342.